A stable partitioned FSI algorithm for rigid bodies and incompressible flow. Part I: Model problem analysis

J. W. Banks[a,2,4], W. D. Henshaw[a,2,3,*], D. W. Schwendeman[a,2,3], Qi Tang[a,1]

[a] *Department of Mathematical Sciences, Rensselaer Polytechnic Institute, Troy, NY 12180, USA.*

Abstract

A stable partitioned algorithm is developed for fluid-structure interaction (FSI) problems involving viscous incompressible flow and rigid bodies. This *added-mass partitioned* (AMP) algorithm remains stable, without sub-iterations, for light and even zero mass rigid bodies when added-mass and viscous added-damping effects are large. The scheme is based on a generalized Robin interface condition for the fluid pressure that includes terms involving the linear acceleration and angular acceleration of the rigid body. Added-mass effects are handled in the Robin condition by inclusion of a boundary integral term that depends on the pressure. Added-damping effects due to the viscous shear forces on the body are treated by inclusion of added-damping tensors that are derived through a linearization of the integrals defining the force and torque. Added-damping effects may be important at low Reynolds number, or, for example, in the case of a rotating cylinder or rotating sphere when the rotational moments of inertia are small. In this first part of a two-part series, the properties of the AMP scheme are motivated and evaluated through the development and analysis of some model problems. The analysis shows when and why the traditional partitioned scheme becomes unstable due to either added-mass or added-damping effects. The analysis also identifies the proper form of the added-damping which depends on the discrete time-step and the grid-spacing normal to the rigid body. The results of the analysis are confirmed with numerical simulations that also demonstrate a second-order accurate implementation of the AMP scheme.

Keywords: fluid-structure interaction, moving overlapping grids, incompressible Navier-Stokes, partitioned schemes, added-mass, rigid bodies

[*]Department of Mathematical Sciences, Rensselaer Polytechnic Institute, 110 8th Street, Troy, NY 12180, USA.
Email addresses: banksj3@rpi.edu (J. W. Banks), henshw@rpi.edu (W. D. Henshaw), schwed@rpi.edu (D. W. Schwendeman), tangq3@rpi.edu (Qi Tang)

[1]Research supported by the Eliza Ricketts Postdoctoral Fellowship.
[2]This work was supported by contracts from the U.S. Department of Energy ASCR Applied Math Program.
[3]Research supported by the National Science Foundation under grant DMS-1519934.
[4]Research supported by a U.S. Presidential Early Career Award for Scientists and Engineers.

Contents

1. Introduction

We consider fluid-structure interaction (FSI) problems involving the motion of rigid bodies in an incompressible fluid. FSI problems of this type occur in a wide variety of applications, such as ones involving particulate flows (suspensions, sedimentation, fluidized beds), valves and moving appendages, buoy structures, ship maneuvering, and underwater vehicles, to name a few. A wide range of numerical techniques have been developed to simulate such FSI problems, including arbitrary Lagrangian–Eulerian (ALE) methods [1–3], methods based on level-sets [4, 5], fictitious domain methods [6–8], embedded boundary methods [9] and immersed boundary methods [10–22].

Numerical schemes for simulating FSI problems can be classified as monolithic or partitioned. Monolithic schemes couple the governing equations for all domains into a single large system. Partitioned schemes make use of separate solvers for the fluid and solid domains with the separate solvers being coupled at fluid-solid interfaces. The choice of discrete interface conditions is one of the primary challenges in developing accurate and stable partitioned schemes. Many partitioned schemes for FSI problems coupling rigid bodies and incompressible flow suffer from numerical instabilities for light bodies. These instabilities usually originate from added-mass and added-damping effects as noted in [2, 11, 15, 16, 19, 22, 23] for example.[5] The dominant instability is often due to added-mass effects that arise from the pressure-induced force and torque on the body. As illustrated in Figure 1, when a force is applied instantaneously to a rigid body in an incompressible fluid, the resultant acceleration of the body depends both on the mass of the body and on the *added-mass* of a portion of the surrounding fluid that is accelerated due to the instantaneous pressure field created by the motion of the body. If the body is heavy, then the effect of the added-mass is small and its associated instability is weak. For light bodies, the added-mass can be significant and lead to added-mass instabilities for partitioned solvers.

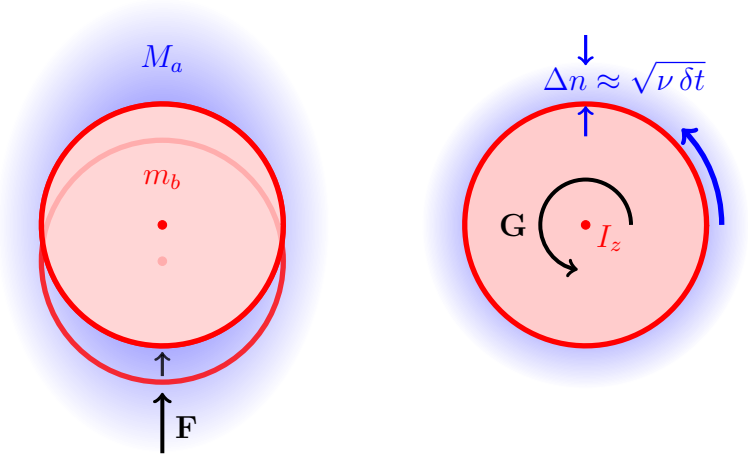

Figure 1: Cartoon illustrating added-mass and added-damping. Left: a force F applied to a rigid-body of mass m_b immersed in an incompressible fluid accelerates a nearby volume of fluid whose mass, the *added-mass* denoted by M_a, contributes to an effective mass of the body. Right: a torque G applied to a rigid disk with moment of inertia I_z over a time interval δt results in a viscous boundary layer of fluid of approximate width $\Delta n \approx \sqrt{\nu\,\delta t}$, where ν is the kinematic viscosity of the fluid. The drag on the surface of the disk associated with this layer leads to an *added-damping* on the rotation of the disk.

A secondary *added-damping* instability may also occur due to the choice of the numerical treatment of the force and torque on the body associated with the viscous shear stress on the surface of the body. Again referring to Figure 1, the resultant angular motion of a rigid disk due to a torque applied about its centre of mass depends both on the moment of inertia of the disk and on the viscous drag created by the fluid in

[5] At the analytic level the notions of added-mass and added-damping have been well known for decades; in a more recent discussion, for example, the form of the added-mass and added-damping is nicely described in Conca et al. [23], where they consider some model problems for which the contributions of added-mass or added-damping in the solutions can be determined explicitly.

a boundary layer near the surface of the disk. The width of this fluid layer grows with time so that it has a damping effect on the motion over an interval of time rather than an instantaneous effect on the acceleration as in the case of added-mass. An implication of this is that instabilities due to added-damping can usually be overcome by taking a sufficiently small time-step (except for the case of a body of zero mass), while added-mass instabilities generally cannot be overcome by taking a smaller time-step if the mass of the body is too small relative to the added-mass.

Implementations of partitioned schemes in the literature based on the traditional coupling between the fluid and solid[6] usually become unstable when the ratio of the density of the solid to that of the fluid is approximately one or less [11, 14]. The common approach to overcome these instabilities is to apply multiple under-relaxed sub-iterations per time-step, often coupled with an acceleration technique such as Aitken's method (e.g., see [3, 14, 20]). However, these sub-iterations can be expensive since a recomputation of the fluid velocity and pressure is required at each iteration, and since a large number of sub-iterations is required when the body is light. In recent years, improving the numerical stability for simulations involving light rigid bodies has attracted considerable attention. For instance, the stability of the immersed boundary method in Uhlmann [11] was improved in the work of Kempe and Fröhlich [16] by explicitly evaluating a volume integral related to the artificial flow field inside the body, which resulted in an improved stability bound to a density ratio of 0.3 or greater. Yang and Stern [19] improved this bound further to 0.1 by relying on a non-iterative immersed boundary approach. They predicated the velocity field in a temporary non-inertial frame that enabled an implicit direct solution of the rigid-body motion and an exact match of the velocity of the fluid and rigid body at the interface. Lacis et al. [22] recently proposed a different non-iterative immersed boundary method that is stable for a density ratio as low as 10^{-4}. Their approach is similar to the block-factorization approach used for similar FSI problems by Fedkiw et al. [24] and Badia et al. [25]. In this approach, an approximate block LU factorization of the discrete monolithic equations is performed that exposes one set of decoupled equations for the fluid velocity and another set of equations that couples the pressure with the motion for the body. This treatment is similar in spirit to the manner that added-mass effects are handled by our new scheme (as described herein), except that our coupling conditions are derived at the continuous level; these continuous conditions are conducive to the development of high-order accurate approximations. Our approach for treating added-damping appears to be new.

The present paper is the first of a two-part series in which we describe a new added-mass/added-damping partitioned approach, referred to as the AMP-RB scheme, for FSI problems involving the motion of rigid bodies in an incompressible flow. The principal feature of the AMP-RB scheme is that it remains stable, without the need for sub-time-step iterations, for FSI problems with light bodies (and even zero-mass bodies) when added-mass and added-damping effects are large. The time-stepping scheme is based on a fractional-step approach for the fluid in which the velocity is advanced in one stage, and the pressure is determined in a second stage [26, 27]. The viscous terms in the stress tensor are handled implicitly so that the velocity can be advanced with a larger stable time step.

The key ingredients of the AMP-RB scheme are contained in the AMP interface conditions which couple the equations of motion of the rigid body to a compatibility boundary condition for the pressure on the surface of the body. These conditions are derived at a continuous level by matching the *acceleration* of the body to that of the fluid. As a result, the integration of the equations of motion of the rigid-body are coupled strongly to the update of the fluid pressure; this ensures the proper balances of forces at the interface thereby suppressing instabilities due to added-mass effects. Suppressing instabilities due to added-damping is more subtle. The fluid forces on the body depend on the viscous shear stresses which, in turn, implicitly depend on the velocity of the body. This implicit dependence of the fluid forces on the body velocity is explicitly exposed and, after some simplifying approximations, is expressed in terms of *added-damping tensors* which are incorporated into the AMP interface conditions as a means to overcome added-damping instabilities.

The work here in Part I focuses on the development of the scheme for two relatively simple model problems, one involving a rectangular geometry and the other posed in an annular domain. The AMP-RB scheme is described fully for the two model problems and the stability of the scheme is analyzed. For the two model problems, it is shown that the scheme is stable (without sub-time-step iterations) for any

[6]The traditional coupling approach, which uses the velocity of the body as a boundary condition on the fluid, and the fluid stress as a boundary condition on the rigid body, is described in Section 3.

ratio of the density of the body to that of the fluid (including the case of a rigid body with zero mass). The present implementation of the numerical scheme is second-order accurate, and this is verified (along with its stability) through a series of test calculations. In Part II [28], the AMP-RB scheme is extended to FSI problems involving more general geometric configurations. This is done using moving overlapping grids [29] to handle more complex fluid domains involving the motion of one or more rigid bodies. Several FSI simulations are performed which also confirm the stability and accuracy of the approach for the general case.

Finally, it is noted that the AMP-RB scheme described here, and its extension in Part II, follows the development of previous AMP schemes for other FSI regimes. These schemes include ones for inviscid compressible fluids coupled to rigid solids [30], linearly elastic solids [31] and nonlinear elastic solids [32], and ones for incompressible fluids coupled to elastic bulk solids [33], elastic structural shells [34] and deforming beams [35]. For all cases, the various AMP schemes are stable for light solids without requiring sub-time-step iterations.

The reminder of the paper is organized as follows. Section 2 defines the governing equations for a rectangular-domain FSI model problem that contains the essential elements needed to address added-mass and added-damping effects. Section 3 defines, in detail, a traditional-partitioned (TP-RB) algorithm in terms of a number of procedures to lay the ground work for describing the changes needed for the new AMP-RB scheme described in the subsequent Section 4. A normal-mode stability analysis of the TP-RB and AMP-RB schemes is performed in Section 5, while Section 6 extends the analysis to a second FSI model problem described in an annular geometry. Numerical verification of the stability and accuracy of the AMP-RB scheme is provided in Section 7. Conclusions of the work in Part I are given in the final Section 8.

2. Governing equations for a FSI model problem

As noted in the introduction, added-mass and added-damping effects arise from the response of the fluid to forces and torques applied to the rigid body. To understand the essential features of these effects with the aim of designing stable numerical methods, it is useful to identify key FSI model problems and then undertake a detailed study of these problems. Consider, for example, the local region near the curved boundary of the rigid body immersed in an incompressible fluid as shown on the left of Figure 2. To derive a suitable FSI model problem for this configuration, we employ a standard mathematical technique and consider a PDE boundary-value problem in a local region near the curved boundary and transform this region to a half plane problem. The transformed half-plane problem is then linearized, the coefficients are frozen, and the lower-order terms are dropped. The result is a model that consists of a rectangular body in the lower half-plane adjacent to an incompressible fluid in the upper-half plane, as shown in the right side of Figure 2. For this FSI problem, added-mass effects arise from a vertical acceleration of the body while added-damping effects occur from a horizontal acceleration. The problem can be simplified further by considering a finite domain and assuming, for example, periodic boundary conditions for the fluid in the horizontal direction and a boundary condition for velocity or pressure of the fluid at a height H in the vertical direction.

Following the prescription outlined above, we consider a first model FSI problem in which the fluid occupies the rectangular domain, $\Omega = [0, L] \times [0, H]$ with coordinates $\mathbf{x} = [x, y]^T$, and lies above a rigid body occupying the region $\Omega_b = [0, L] \times [-\bar{H}, 0]$, see Figure 3. The fluid in Ω has velocity, $\mathbf{v}(\mathbf{x}, t) = [u(\mathbf{x}, t), v(\mathbf{x}, t)]^T$, and pressure, $p(\mathbf{x}, t)$, and is taken to be viscous and incompressible. It is assumed that the rigid body undergoes small displacements in the x or y-direction, but does not rotate, and that the interface separating the fluid and the rigid body is linearized about the fixed portion of the x-axis given by $\Gamma_b = [0, L] \times \{0\}$. The velocity and acceleration of the body are denoted by $\mathbf{v}_b(t) = [u_b(t), v_b(t)]^T$ and $\dot{\mathbf{v}}_b(t) = \mathbf{a}_b(t) = [a_u(t), a_v(t)]^T$, respectively, and the motion of the body is connected to that of the fluid by

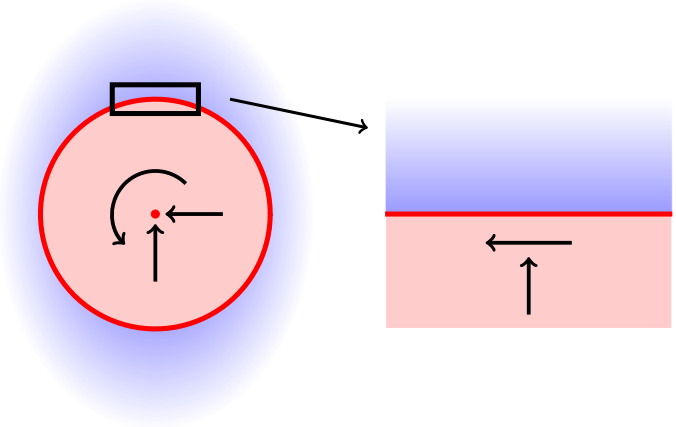

Figure 2: Prototypical added-mass and added-damping problems are derived from localizing the problem on the left near the boundary of the rigid body. This leads to the simplified rectangular-geometry problem on the right for which added-mass effects arise due to vertical motions while added-damping effects arise from horizontal translations.

conditions on velocity and stress along Γ_b. The full set of equations governing the model problem are

$$\begin{aligned}
\text{Fluid:} \quad & \rho\frac{\partial \mathbf{v}}{\partial t} + \nabla p = \mu\Delta\mathbf{v}, && \mathbf{x}\in\Omega, && (1)\\
& \nabla\cdot\mathbf{v} = 0, && \mathbf{x}\in\Omega, && (2)\\
\text{Rigid body:} \quad & m_b\, a_u = \int_0^L \mu\frac{\partial u}{\partial y}(x,0,t)\,dx + g_u(t), && && (3)\\
& m_b\, a_v = -\int_0^L p(x,0,t)\,dx + g_v(t), && && (4)\\
\text{Interface:} \quad & \mathbf{v}(x,0,t) = \mathbf{v}_b(t), && x\in[0,L], && (5)\\
\text{Top fluid BCs:} \quad & u(x,H,t) = u_H(x,t), && x\in[0,L], && (6)\\
& p(x,H,t) = p_H(x,t), && x\in[0,L], && (7)\\
\text{Side fluid BCs:} \quad & \mathbf{v}(0,y,t) = \mathbf{v}(L,y,t), && y\in[0,H]. && (8)
\end{aligned}$$

Here, ρ is the constant fluid density, μ is the constant fluid viscosity, m_b is the mass of the rigid body, and $g_u(t)$ and $g_v(t)$ are external forces on the rigid body in the horizontal and vertical directions, respectively. These equations are augmented with appropriate initial conditions.

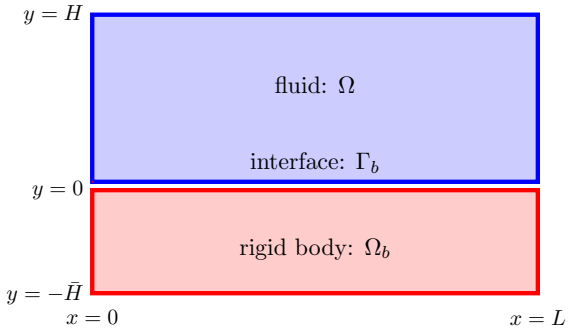

Figure 3: The geometry for the rectangular geometry FSI model problems.

An elliptic equation for the fluid pressure can be derived by taking the divergence of the momentum equation in (1) and using the continuity equation in (2) to give

$$\Delta p = 0, \qquad \mathbf{x}\in\Omega. \tag{9}$$

In the velocity-pressure form of the Stokes equations, the momentum equation for the velocity in (1) is used with the Laplace equation for the pressure in (9) instead of the divergence equation in (2). To retain consistency with the original velocity-divergence form of the equations, zero divergence is specified as an additional boundary condition, i.e. $\nabla \cdot \mathbf{v} = 0$ for $\mathbf{x} \in \partial\Omega$, see [26] for additional details.

In the discussion to follow we use a fractional-step method based on the velocity-pressure form of the fluid equations to define partitioned FSI algorithms. In Section 3 a traditional partitioned scheme, referred to as the TP-RB algorithm, is described. Then in Section 4 we present our new *added-mass partitioned* scheme which will be referred to as the AMP-RB algorithm. The important difference in the two approaches lies in the coupling of the fractional-step method for the fluid with the equations governing the motion of the body.

3. Traditional Partitioned/Rigid-Body algorithm TP-RB

We begin our discussion of partitioned algorithms for the rectangular model FSI problem by considering a *traditional partitioned* scheme. This is done to establish the basic elements of a partitioned FSI algorithm based on a fractional-step time-stepping scheme for the velocity-pressure formulation of the fluid equations and to lay the groundwork for a later discussion of the new *added-mass partitioned* scheme.

To set some notation, let $\mathbf{x_i}$ denote the grid-point coordinates of a mesh covering the fluid domain, $\mathbf{x} \in \Omega$, where $\mathbf{i} = (i_1, i_2)$ is a multi-index, and let $\mathbf{i} \in \Omega_h$ denote the set of indices of points in the interior of the fluid grid while $\mathbf{i} \in \Gamma_h$ are the indices of points on the interface, $\mathbf{x} \in \Gamma_b$. Grid functions for the fluid velocity and pressure are given by $\mathbf{v}_\mathbf{i}^n \approx \mathbf{v}(\mathbf{x_i}, t^n)$ and $p_\mathbf{i}^n \approx p(\mathbf{x_i}, t^n)$, respectively, where $t^n = n\Delta t$, $n = 0, 1, 2, \ldots$, denote discrete times with time step Δt. The rigid-body displacement, velocity, and acceleration at discrete times are given by $\mathbf{x}_b^n \approx \mathbf{x}_b(t^n)$, $\mathbf{v}_b^n \approx \mathbf{v}_b(t^n)$, and $\mathbf{a}_b^n \approx \mathbf{a}_b(t^n)$ respectively. Second-order accurate approximations are used for the spatial operators in (1), (2) and (9), and we denote these discrete approximations using a subscript h. Precise definitions for these approximations are not important in the present discussion. In describing the algorithm, $\mathbf{v}_\mathbf{i}^n$, $p_\mathbf{i}^n$, $\mathbf{v}_b^n$ and $\mathbf{a}_b^n$ are assumed to be known at t^n and t^{n-1}, and the output is the discrete solution at t^{n+1}.

The TP-RB time-stepping scheme is described in Algorithm 1, and uses four procedures which are defined below. The resulting scheme is formally second-order accurate in both space and time, using either the predicted values as the solution at t^{n+1}, or the discrete solution after the correction steps. Generally, the predictor-corrector scheme has favorable stability properties in comparison to the scheme using the prediction steps alone, but in either case the algorithm suffers from instabilities when added-mass or added-damping effects are significant. This occurs when the ratio of the mass of the rigid body to that of the fluid contained in Ω is too small as shown in Sections 5.1 and 5.2. The added-mass/added-damping instabilities can be suppressed by coupling the calculation of the fluid pressure and the rigid-body acceleration as discussed in the next section.

Procedure $(\,\mathbf{a}_b\,,\,\mathbf{v}_b\,) =$ **predictAndExtrapRigidBody**$(\,\mathbf{a}_b^n\,,\,\mathbf{a}_b^{n-1}\,,\,\mathbf{v}_b^{n-1}\,)$

Compute provisional values $(\mathbf{a}_b, \mathbf{v}_b)$ for the acceleration and velocity of the rigid body at t^{n+1} using a linear extrapolation in time for the acceleration followed by a leap-frog integration for the velocity:

$$\begin{aligned} \mathbf{a}_b &= 2\mathbf{a}_b^n - \mathbf{a}_b^{n-1}, \\ \mathbf{v}_b &= \mathbf{v}_b^{n-1} + 2\Delta t\, \mathbf{a}_b^n. \end{aligned}$$

Procedure $(\,\mathbf{v_i}\,) =$ **advanceFluidVelocity**$(\,\mathbf{v}_b^*\,,\,p_\mathbf{i}^*\,,\,p_\mathbf{i}^n\,,\,\mathbf{v}_\mathbf{i}^n\,)$

Advance the fluid velocity $\mathbf{v_i}$ to t^{n+1} using a second-order accurate semi-implicit scheme for the momentum equation in (1):

$$\begin{aligned} &\rho\frac{\mathbf{v_i} - \mathbf{v}_\mathbf{i}^n}{\Delta t} + \frac{1}{2}\nabla_h p_\mathbf{i}^* + \frac{1}{2}\nabla_h p_\mathbf{i}^n = \frac{\mu}{2}\Big(\Delta_h \mathbf{v_i} + \Delta_h \mathbf{v}_\mathbf{i}^n\Big), && \mathbf{i} \in \Omega_h, \\ &\mathbf{v_i} = \mathbf{v}_b^*, \quad \nabla_h \cdot \mathbf{v_i} = 0, && \mathbf{i} \in \Gamma_h. \end{aligned}$$

Algorithm 1 Traditional partitioned (TP-RB) scheme

// Preliminary body evolution step

1. $(\mathbf{a}_b^{(e)}, \mathbf{v}_b^{(e)}) = \textbf{predictAndExtrapRigidBody}(\mathbf{a}_b^n, \mathbf{a}_b^{n-1}, \mathbf{v}_b^{n-1})$

// Prediction steps

2. $(\mathbf{v}_\mathbf{i}^{(p)}) = \textbf{advanceFluidVelocity}(\mathbf{v}_b^{(e)}, 2p_\mathbf{i}^n - p_\mathbf{i}^{n-1}, p_\mathbf{i}^n, \mathbf{v}_\mathbf{i}^n)$
3. $(p_\mathbf{i}^{(p)}) = \textbf{updateFluidPressure}(\mathbf{v}_\mathbf{i}^{(p)}, \mathbf{a}_b^{(e)})$
4. $(\mathbf{v}_b^{(p)}, \mathbf{a}_b^{(p)}) = \textbf{advanceBodyVelocityAndAcceleration}(\mathbf{v}_b^n, \mathbf{a}_b^n, \mathbf{v}_\mathbf{i}^{(p)}, p_\mathbf{i}^{(p)})$

// Correction steps

5. $(\mathbf{v}_\mathbf{i}^{n+1}) = \textbf{advanceFluidVelocity}(\mathbf{v}_b^{(p)}, p_\mathbf{i}^{(p)}, p_\mathbf{i}^n, \mathbf{v}_\mathbf{i}^n)$
6. $(p_\mathbf{i}^{n+1}) = \textbf{updateFluidPressure}(\mathbf{v}_\mathbf{i}^{n+1}, \mathbf{a}_b^{(p)})$
7. $(\mathbf{v}_b^{n+1}, \mathbf{a}_b^{n+1}) = \textbf{advanceBodyVelocityAndAcceleration}(\mathbf{v}_b^n, \mathbf{a}_b^n, \mathbf{v}_\mathbf{i}^{n+1}, p_\mathbf{i}^{n+1})$

In this procedure, the viscous term for the velocity is computed using an implicit trapezoidal method, while the pressure gradient uses a predicted value for the pressure at t^{n+1} given by $p_\mathbf{i}^*$ so that this term is explicit. A discrete approximation of the continuity equation is used to determine the vertical (normal) component of the velocity in the ghost points associated with the interface $\mathbf{i} \in \Gamma_h$, while the horizontal (tangential) component of the velocity is determined in the ghost points using extrapolation. Discrete boundary conditions are also applied at the boundary of the mesh corresponding to $y = H$, as well as periodic conditions along the sides corresponding to $x = 0$ and $x = L$.

Procedure $(p_\mathbf{i}) = \textbf{updateFluidPressure}(\mathbf{v}_\mathbf{i}^*, \mathbf{a}_b^*)$

Update the fluid pressure $p_\mathbf{i}$ at t^{n+1} by solving a discrete Laplace equation for the pressure

$$\Delta_h p_\mathbf{i} = 0, \qquad \mathbf{i} \in \Omega_h \cup \Gamma_h, \tag{10}$$

together with the interface condition

$$D_{yh}\, p_\mathbf{i} = -\rho a_v^* - \mu \nabla_h \times \nabla_h \times v_\mathbf{i}^*, \qquad \mathbf{i} \in \Gamma_h, \tag{11}$$

which is derived from the y-component of the momentum equation for the fluid velocity.[7] Here, D_{yh} is a second-order accurate approximation to the y-derivative at the interface, and $\mathbf{v}_\mathbf{i}^*$ and $\mathbf{a}_b^*$ are predicted values for the fluid velocity and the acceleration of the body, respectively, at t^{n+1}. Periodic boundary conditions are applied on $x_\mathbf{i} = 0$ and L, and appropriate boundary conditions are applied on $y_\mathbf{i} = H$.

Procedure $(\mathbf{v}_b, \mathbf{a}_b) = \textbf{advanceBodyVelocityAndAcceleration}(\mathbf{v}_b^n, \mathbf{a}_b^n, \mathbf{v}_\mathbf{i}^*, p_\mathbf{i}^*)$

Compute the rigid-body acceleration $\mathbf{a}_b$ at t^{n+1} by solving discrete approximations of the rigid-body equa-

[7] The term Δv from the y-component of (1) has been replaced by $-\nabla \times \nabla \times v$ to avoid a viscous time-step restriction in the application of the discrete interface condition in (11), see [36] for additional details.

tions in (3) and (4) given by

$$a_u = \frac{1}{m_b}\left\{\sum_{\mathbf{i}\in\Gamma_h} \mu\big(D_{yh}\, u^*_{\mathbf{i}}\big)\Delta x + g_u(t^{n+1})\right\}, \tag{12}$$

$$a_v = \frac{1}{m_b}\left\{-\sum_{\mathbf{i}\in\Gamma_h} p^*_{\mathbf{i}}\,\Delta x + g_v(t^{n+1})\right\}, \tag{13}$$

and then advance the rigid-body velocity $\mathbf{v}_b$ *using the trapezoidal method*

$$\mathbf{v}_b = \mathbf{v}_b^n + \frac{\Delta t}{2}\big(\mathbf{a}_b + \mathbf{a}_b^n\big).$$

Here, $\mathbf{v}^*_{\mathbf{i}}$ *and* $p^*_{\mathbf{i}}$ *are computed grid functions for the fluid velocity and pressure, respectively, at* t^{n+1}.

4. Added-Mass Partitioned/Rigid-Body algorithm AMP-RB

In this section we develop the AMP-RB algorithm for the FSI model problem given in (1)–(8). Before defining the algorithm, we first describe the key interface conditions that are used to account for the added-mass and added-damping effects. The simplified interface conditions described here are a special case of the more general conditions discussed in Part II [28]. The simplified conditions motivate the more general conditions and also illustrate the key ideas behind the AMP approach for incompressible flows and rigid bodies. The resulting AMP algorithm for the model problem retains the essential characteristics of the general AMP scheme described in Part II, but is simpler to describe and analyze.

4.1. Added-mass interface conditions

In the model problem described in Section 2, added-mass effects arise in (4) from the force on the rigid body due to the fluid pressure through the integral term

$$\mathcal{I}_p(p, a_v) \stackrel{\text{def}}{=} -\int_0^L p(x, 0, t)\, dx. \tag{14}$$

Notice that the integral depends on the fluid pressure, p, but the pressure, in turn, is an implicit function of the vertical acceleration of the body, a_v, through the coupled motion of the fluid and the body. Therefore one may regard the integral in (14) to be a function of p and a_v. The contribution to the added-mass from this integral term is revealed by matching the vertical *acceleration* of the fluid and body on the interface,

$$\frac{\partial v}{\partial t} = \frac{dv_b}{dt} = a_v, \quad \mathbf{x} \in \Gamma, \tag{15}$$

which follows from the time derivative of the vertical component of the interface condition in (5). Combining (15) with the y-component of the fluid momentum equation in (1) implies the two coupled interface conditions given by

$$\rho a_v + \frac{\partial p}{\partial y} = \mu \Delta v, \qquad \mathbf{x} \in \Gamma, \tag{16}$$

$$m_b\, a_v = \mathcal{I}_p(p, a_v) + g_v(t). \tag{17}$$

In the AMP-RB algorithm described below, equations (16) and (17) are used as interface conditions when solving the Laplace equation for the fluid pressure (with v on the left-hand side of (16) assumed to be given by a previous step in the algorithm). We note that the vertical acceleration of body, a_v, in (16) can be viewed as a Lagrange multiplier that is adjusted to enforce the scalar constraint given by (17). In this formulation, the vertical component of the acceleration of the body is determined with the fluid pressure in the solution of the elliptic problem, and the key idea is that this can be done when m_b is small, or even zero.

Note that when $m_b \neq 0$, the vertical component of the acceleration, a_v, can be eliminated from (16) and (17) to give a generalized Robin condition on the pressure

$$\frac{m_b}{\rho}\frac{\partial p}{\partial y} + \int_0^L p\,dx = \frac{m_b}{\rho}\,\mu\Delta v + g_v(t), \qquad \mathbf{x} \in \Gamma. \tag{18}$$

Use of (18), however, is not valid as the only boundary condition for the pressure when $m_b = 0$ since only one independent condition remains; furthermore (18) may be poorly conditioned in the numerical scheme when m_b is very small.

4.2. Added-damping interface conditions

Added-damping effects arise primarily due to viscous shear forces on the body, and in the model problem of Section 2 these are associated with the integral of the shear stress given by

$$\mathcal{I}_u(u, u_b) \stackrel{\text{def}}{=} \int_0^L \mu\frac{\partial u}{\partial y}(x, 0, t)\,dx, \tag{19}$$

which determines the horizontal force on the body in (3). Here $\mathcal{I}_u$ can be considered to be a function of the horizontal components of the velocity of the fluid and the body since u is an implicit function of u_b. In order to suppress added-damping effects in the AMP-RB algorithm, it is important to reveal the dependence of $\mathcal{I}_u$ on the velocity u_b (or more specifically the acceleration a_u), at least in an approximate sense. Let us assume that predicted values for the velocities, $u^{(p)}$ and $u_b^{(p)}$, are available and consider the linear approximation

$$\begin{aligned}\mathcal{I}_u(u, u_b) &\approx \mathcal{I}_u(u^{(p)}, u_b^{(p)}) + \left(\frac{\partial \mathcal{I}_u}{\partial u_b}\right)^{(p)} \big(u_b - u_b^{(p)}\big),\\ &= \mathcal{I}_u(u^{(p)}, u_b^{(p)}) - \mathcal{D}^u\big(u_b - u_b^{(p)}\big),\end{aligned} \tag{20}$$

where $\mathcal{D}^u$ is the *added-damping coefficient*[8] defined by

$$\mathcal{D}^u \stackrel{\text{def}}{=} -\frac{\partial \mathcal{I}_u}{\partial u_b}. \tag{21}$$

A formula for $\mathcal{D}^u$ can be found by considering a suitable variational problem associated with the FSI model problem as is discussed later in Section 5.2.2.

In practice, it is convenient to work with the acceleration a_u, instead of the velocity u_b, which suggests an alternate linearization of the form

$$\mathcal{I}_u(u, u_b) \approx \mathcal{I}_u(u^{(p)}, u_b^{(p)}) - \beta_d\,\Delta t\,\mathcal{D}^u\,\big(a_u - a_u^{(p)}\big), \tag{22}$$

where $a_u^{(p)}$ is a predicted acceleration of the body (note the factor of Δt) and where we have introduced the *added-damping parameter* β_d, whose value plays an important role in the stability of the AMP-RB scheme.

Definition 1. Added-damping parameter β_d. *The parameter β_d is called the added-damping parameter and is a free parameter that multiplies the added-damping coefficient $\mathcal{D}^u$ in the linearization of the integral of the shear stress.*

A stability analysis of the AMP-RB algorithm applied to an *added-damping* model problem reveals a range of stable values for β_d (see Section 5.2.3). For now, we note that the linearization in (22) is an important element in the AMP-RB algorithm since it enables a stable calculation of the horizontal acceleration of the body, a_u, in (3) even when m_b is small, or even zero, i.e. when added-damping effects are significant.

[8] For more general FSI problems, $\mathcal{D}^u$ takes the form of an *added-damping tensor*, see Part II [28].

4.3. AMP-RB algorithm

We are now in a position to describe the AMP-RB algorithm for the FSI model problem. As in the TP-RB algorithm, the fluid is advanced using a fractional-step method based on the velocity-pressure form of the equations. While this approach is common to both algorithms, there are important differences. The principal difference is that the AMP-RB algorithm uses the interface conditions in (16) and (17) for added-mass, and the condition in (22) for added-damping in the stage involving the elliptic problem for the fluid pressure. Thus, the pressure and the acceleration of the rigid body are determined *together* in one stage of the AMP-RB algorithm, while the velocity of the body is advanced in time in a subsequent stage.

Algorithm 2 Added-mass partitioned (AMP-RB) scheme

// Preliminary body evolution step

1. $(\mathbf{a}_b^{(e)}, \mathbf{v}_b^{(e)}) = \textbf{predictAndExtrapRigidBody}(\mathbf{a}_b^n, \mathbf{a}_b^{n-1}, \mathbf{v}_b^{n-1})$

// Prediction steps

2. $(\mathbf{v}_{\mathbf{i}}^{(p)}) = \textbf{advanceFluidVelocity}(\mathbf{v}_b^{(e)}, 2p_{\mathbf{i}}^n - p_{\mathbf{i}}^{n-1}, p_{\mathbf{i}}^n, \mathbf{v}_{\mathbf{i}}^n)$
3. $(p_{\mathbf{i}}^{(p)}, \mathbf{a}_b^{(p)}) = \textbf{updateFluidPressureAndBodyAcceleration}(\mathbf{v}_{\mathbf{i}}^{(p)}, \mathbf{a}_b^{(e)})$
4. $(\mathbf{v}_b^{(p)}) = \textbf{advanceBodyVelocityOnly}(\mathbf{a}_b^{(p)}, \mathbf{a}_b^n, \mathbf{v}_b^n)$

// Correction steps

5. $(\mathbf{v}_{\mathbf{i}}^{n+1}) = \textbf{advanceFluidVelocity}(\mathbf{v}_b^{(p)}, p_{\mathbf{i}}^{(p)}, p_{\mathbf{i}}^n, \mathbf{v}_{\mathbf{i}}^n)$
6. $(p_{\mathbf{i}}^{n+1}, \mathbf{a}_b^{n+1}) = \textbf{updateFluidPressureAndBodyAcceleration}(\mathbf{v}_{\mathbf{i}}^{n+1}, \mathbf{a}_b^{(p)})$
7. $(\mathbf{v}_b^{n+1}) = \textbf{advanceBodyVelocityOnly}(\mathbf{a}_b^{n+1}, \mathbf{a}_b^n, \mathbf{v}_b^n)$

// Fluid-velocity correction step (optional)

8. $(\mathbf{v}_{\mathbf{i}}^{n+1}) = \textbf{advanceFluidVelocity}(\mathbf{v}_b^{n+1}, p_{\mathbf{i}}^{n+1}, p_{\mathbf{i}}^n, \mathbf{v}_{\mathbf{i}}^n)$

The AMP-RB algorithm is given in Algorithm 2, and uses two procedures introduced in Section 3 as well as two additional procedures defined below. The AMP-RB algorithm uses a similar predictor-corrector time-stepping approach as in the TP-RB algorithm, and it is also second-order accurate in space and time. For the AMP-RB algorithm, we have included an optional fluid *velocity correction* (VC) step which serves to adjust the fluid velocity so that it exactly matches the velocity of the body along the interface at t^{n+1}. In practice, we have found that this step, which requires an additional implicit solve for the velocity, is only needed for difficult problems with strong added-mass and added-damping effects as we show in Section 5.2.3. Also, it is possible to repeat the correction group of procedures multiple times, but in practice we only use one correction group.

Procedure $(p_{\mathbf{i}}, \mathbf{a}_b) = \textbf{updateFluidPressureAndBodyAcceleration}(\mathbf{v}_{\mathbf{i}}^*, \mathbf{a}_b^*)$

Update the fluid pressure $p_{\mathbf{i}}$ and the rigid-body acceleration a_v at t^{n+1} by solving a discrete Laplace equation for the pressure in (10) together with the discrete AMP interface conditions

$$D_{yh}\, p_{\mathbf{i}} + \rho a_v = -\mu \nabla_h \times \nabla_h \times v_{\mathbf{i}}^*, \qquad \mathbf{i} \in \Gamma_h, \tag{23}$$

$$m_b a_v + \sum_{\mathbf{i}\in\Gamma_h} p_{\mathbf{i}} \Delta x = g_v(t^{n+1}), \tag{24}$$

$$[m_b + \beta_d\, \Delta t\, \mathcal{D}^u]\, a_u = \sum_{\mathbf{i}\in\Gamma_h} \mu\big(D_{yh}\, u_{\mathbf{i}}^*\big)\Delta x + \beta_d\, \Delta t\, \mathcal{D}^u\, a_u^* + g_u(t^{n+1}), \tag{25}$$

which are approximations of the interface conditions in (16), (17) and (22). Here $\mathcal{D}^u$ is the added-damping coefficient and β_d is the added-damping parameter introduced in Section 4.2. As before, D_{yh}

is a second-order accurate approximation to the y-derivative, and $\mathbf{v}_{\mathbf{i}}^*$ *and* $\mathbf{a}_b^*$ *are predicted values for the fluid velocity and the acceleration of the body, respectively, at* t^{n+1}*. Periodic boundary conditions are applied on* $x_{\mathbf{i}} = 0$ *and* L*, and appropriate boundary conditions are applied on* $y_{\mathbf{i}} = H$*.*

For the model problem considered here, we note that the discrete pressure, $p_{\mathbf{i}}$, and the vertical component of the rigid body acceleration, a_v, are coupled and determined by the solution to the elliptic problem consisting of the discrete Laplace equation in (10) with interface conditions in (23) and (24), while the horizontal component of the rigid body, a_u, is determined independently by the interface condition in (25). However, for FSI problems with general curved interfaces, these equations for the pressure and body accelerations are fully coupled, see Part II for more details.

Procedure $(\mathbf{v}_b) =$ **advanceBodyVelocityOnly**$(\mathbf{a}_b^*, \mathbf{a}_b^n, \mathbf{v}_b^n)$

Advance the rigid-body velocity $\mathbf{v}_b$ *to* t^{n+1} *using the trapezoidal method*

$$\mathbf{v}_b = \mathbf{v}_b^n + \frac{\Delta t}{2}\big(\mathbf{a}_b^* + \mathbf{a}_b^n\big),$$

using a computed value for the rigid-body $\mathbf{a}_b^*$ *at* t^{n+1}*.*

5. Stability analyses of the AMP-RB and TP-RB schemes for FSI model problems

The stability properties of the AMP-RB and TP-RB algorithms can be understood by considering two sub-problems derived from the FSI model problem given in (1)–(8). The first problem focuses on the effects of added-mass, while the second problem reveals issues associated with added-damping. A derivation of the two problems begins with a Fourier analysis of the periodic solution for the fluid variables. Let $\hat{u}_k(y,t)$, $\hat{v}_k(y,t)$ and $\hat{p}_k(y,t)$ denote coefficient functions of the Fourier series in the x-direction for the components of the fluid velocity and the pressure. For example, $\hat{u}_k(y,t)$ is defined by

$$u(x,y,t) = \sum_{k=-\infty}^{\infty} \hat{u}_k(y,t) e^{2\pi i k x/L}\ , \tag{26}$$

with similar formulas defining $\hat{v}_k(y,t)$ and $\hat{p}_k(y,t)$. The equations governing the coefficient functions for the $k = 0$ mode of the fluid, together with the equations and interface conditions for the rigid-body velocity, decouple into the two sub-problems, one for the pressure and the components of fluid and rigid-body velocity in the vertical direction, and the other the components of the velocity in the horizontal direction. It is the problem for the pressure and vertical components of velocity that forms the model for added-mass effects, with the other problem being the model for added damping. The problem for added mass, called MP-AM, is discussed in detail in Section 5.1, while a discussion of the problem for added damping, called MP-AD, is given in Section 5.2.

We note that the problems for the other Fourier-modes with $k \neq 0$ satisfy homogeneous Dirichlet conditions at the interface and do not couple to the motion of the rigid body. Since these modes are not coupled to the motion of the rigid body, they are therefore not germane to our discussion of instabilities related to added-mass or added-damping effects and will not be considered further here.

5.1. Analysis of a model problem for added mass

A model problem describing the added-mass effect is first derived. Subsequently, stability analyses of the TP-RB and AMP-RB schemes to solve this model problem are given.

5.1.1. Added-mass model problem MP-AM

The added-mass model problem is obtained from the $k = 0$ mode in the Fourier expansion of the fluid variables together with the equation for the vertical component of the rigid body. This model problem for

added mass (MP-AM) is given by

$$\text{MP-AM:}\quad \begin{cases} \rho\dfrac{\partial \hat{v}}{\partial t} + \dfrac{\partial \hat{p}}{\partial y} = 0, & y \in (0,H), \\ \dfrac{\partial \hat{v}}{\partial y} = 0, & y \in (0,H), \\ m_b \dfrac{dv_b}{dt} = -L\,\hat{p}(0,t) + g_v(t), & \\ \hat{v}(0,t) = v_b, \quad \hat{p}(H,t) = \hat{p}_H(t), & \end{cases} \tag{27}$$

where the subscript on the coefficient functions corresponding to $k = 0$ has been dropped for notational convenience. The solution of the model problem is

$$v_b(t) = \frac{1}{m_b + M_a}\int_0^t \Big[g_v(\tau) - L\hat{p}_H(\tau)\Big]\,d\tau \; + v_b(0), \tag{28}$$

$$\hat{p}(y,t) = \hat{p}_H(t) + \Big(1 - \frac{y}{H}\Big)\,\frac{g_v(t)/L - \hat{p}_H(t)}{m_b/M_a + 1}, \tag{29}$$

$$\hat{v}(t) = v_b(t), \tag{30}$$

where

$$M_a = \rho L H, \tag{31}$$

is the added mass for this problem and corresponds to the mass of the fluid in the whole rectangular domain. Note that the fluid velocity, $\hat{v}$, which only depends on time and not space, is equal to the velocity of the rigid body according to the condition at the interface, $y = 0$. Meanwhile, the fluid pressure, $\hat{p}$, is a linear function of y with time-dependent forcing. The acceleration of the body is given by

$$a_v(t) = \frac{dv_b}{dt} = \frac{g_v(t) - L\hat{p}_H(t)}{m_b + M_a}, \tag{32}$$

which is the total (time-dependent) force applied to the body divided by the sum of its mass, m_b, and the added mass, M_a. Importantly, the acceleration is seen to be bounded, even when $m_b = 0$, assuming that the external forcing is bounded and that M_a is bounded away from zero.

5.1.2. Analysis of the TP-RB algorithm for MP-AM

A stability analysis of the TP-RB time-stepping scheme in Algorithm 1 for the MP-AM model problem is now presented. For this added-mass model problem, the fully discretized scheme simplifies to the one described in detail in Algorithm 3. Here, $\hat{v}_j^n$ and $\hat{p}_j^n$ approximate $\hat{v}(y,t)$ and $\hat{p}(y,t)$, respectively, at $y_j = j\Delta y$ and $t^n = n\Delta t$, and v_b^n and a_v^n approximate $v_b(t)$ and $a_v(t)$, respectively, at t^n. The symbols D_0, D_+ and D_- denote centred, forward and backward divided difference operators, respectively, defined by

$$D_0\hat{p}_j^n \stackrel{\text{def}}{=} \frac{\hat{p}_{j+1}^n - \hat{p}_{j-1}^n}{2\Delta y}, \qquad D_+\hat{p}_j^n \stackrel{\text{def}}{=} \frac{\hat{p}_{j+1}^n - \hat{p}_j^n}{\Delta y}, \qquad D_-\hat{p}_j^n \stackrel{\text{def}}{=} \frac{\hat{p}_j^n - \hat{p}_{j-1}^n}{\Delta y}, \tag{33}$$

while D_{yh} is a second-order accurate one-sided approximation of the first derivative given by

$$D_{yh}\hat{p}_j^n = \frac{-3\hat{p}_j^n + 4\hat{p}_{j+1}^n - \hat{p}_{j+2}^n}{2\Delta y}. \tag{34}$$

For the stability analysis of this scheme, it is convenient to consider the homogeneous equations with zero forcing so that the discrete variables appearing in the various steps of the algorithm are regarded as *perturbations* to the exact discrete solution. The objective of the analysis is then to determine under what conditions the perturbations can be bounded.

The first two steps in Algorithm 3 result in preliminary values for the velocity and acceleration of the rigid body as well as a predicted value for the fluid velocity. Of primary interest is the extrapolated value

Algorithm 3 TP-RB scheme for MP-AM

Added-mass model problem in a rectangular geometry.

// Preliminary body evolution step

1. $a_v^{(e)} = 2a_v^n - a_v^{n-1}, \qquad v_b^{(e)} = v_b^{n-1} + 2\Delta t\, a_v^n,$

// Prediction steps

2. $\hat{v}_j^{(p)} = \hat{v}_j^n - \frac{3\Delta t}{2\rho} D_0 \hat{p}_j^n + \frac{\Delta t}{2\rho} D_0 \hat{p}_j^{n-1}, \quad j = 1, 2, \ldots, N, \qquad \hat{v}_0^{(p)} = v_b^{(e)}, \quad D_0 \hat{v}_N^{(p)} = 0,$
3. $D_+ D_- \hat{p}_j^{(p)} = 0, \quad j = 1, 2, \ldots, N-1, \qquad D_{yh} \hat{p}_0^{(p)} = -\rho a_v^{(e)}, \quad \hat{p}_N^{(p)} = \hat{p}_H(t^{n+1}),$
4. $a_v^{(p)} = (-L\hat{p}_0^{(p)} + g_v(t^{n+1}))/m_b, \qquad v_b^{(p)} = v_b^n + \frac{\Delta t}{2}(a_v^{(p)} + a_v^n),$

// Correction steps

5. $\hat{v}_j^{n+1} = \hat{v}_j^n - \frac{\Delta t}{2\rho}(D_0 \hat{p}_j^{(p)} + D_0 \hat{p}_j^n), \quad j = 1, 2, \ldots, N, \qquad \hat{v}_0^{n+1} = v_b^{(p)}, \quad D_0 \hat{v}_N^{n+1} = 0,$
6. $D_+ D_- \hat{p}_j^{n+1} = 0, \quad j = 1, 2, \ldots, N-1, \qquad D_{yh} \hat{p}_0^{n+1} = -\rho a_v^{(p)}, \quad \hat{p}_N^{n+1} = \hat{p}_H(t^{n+1}),$
7. $a_v^{n+1} = (-L\hat{p}_0^{n+1} + g_v(t^{n+1}))/m_b, \qquad v_b^{n+1} = v_b^n + \frac{\Delta t}{2}(a_v^{n+1} + a_v^n),$

for the vertical component of the acceleration given by

$$a_v^{(e)} = 2a_v^n - a_v^{n-1}. \tag{35}$$

This extrapolated value for the acceleration appears in the boundary condition of the elliptic problem for $\hat{p}_j^{(p)}$ in Step 3, whose solution is linear in y and takes the form

$$\hat{p}_j^{(p)} = -\rho a_v^{(e)}\big(y_j - H\big), \qquad j = 0, 1, \ldots, N, \tag{36}$$

where $a_v^{(e)}$ is given in (35). The solution for the pressure perturbation in (36) evaluated at $y_0 = 0$ is used in Step 4 to compute the vertical component of the acceleration of the body. With the forcing set to zero, we find

$$a_v^{(p)} = -\frac{L\hat{p}_0^{(p)}}{m_b} = -\left(\frac{\rho LH}{m_b}\right) a_v^{(e)}, \tag{37}$$

where (36) has been used to eliminate $\hat{p}_0^{(p)}$. The velocity of the body, $v_b^{(p)}$, is also computed at this step of the algorithm, but its value does not play an important role in the stability analysis.

The final group of correction steps in Algorithm 3 consists of a fluid velocity correction, Step 5, a second fluid pressure update, Step 6, and a final correction of the vertical components of the rigid-body velocity and acceleration, Step 7. Note that since $\hat{p}_j^{(p)}$ is linear in y_j, the pressure gradient terms in the discrete momentum equation in Step 5 is constant in j so that this step reduces to setting the (spatially uniform) fluid velocity, $\hat{v}_j^{n+1}$, equal to the body velocity, $v_b^{(p)}$, computed in Step 4. The solution for the discrete fluid pressure, $\hat{p}_j^{n+1}$, in Step 6 gives the solution in (36) but with $a_v^{(e)}$ replaced by the predicted value, $a_v^{(p)}$, given in (37). Using this solution for the pressure and the value for $a_v^{(e)}$ in (35), the vertical component of the acceleration of the body at t^{n+1} becomes

$$a_v^{n+1} = \frac{2a_v^n - a_v^{n-1}}{M_r^2}, \tag{38}$$

where

$$M_r = \frac{m_b}{\rho LH} = \frac{m_b}{M_a}, \tag{39}$$

is the ratio of the mass of the rigid body to the added mass, M_a. The vertical component of the velocity of

the body is computed at this final step to be

$$v_b^{n+1} = v_b^n + \frac{\Delta t}{2}\left(a_v^{n+1} + a_v^n\right). \tag{40}$$

The behaviour of the perturbations in the rigid-body acceleration and velocity for the TP-RB algorithm applied to the model problem, MP-MA, are given by (38) and (40), respectively, with the perturbations in the fluid velocity and pressure determined by the rigid-body perturbations through the velocity equilibration in Step 5 and the pressure solve in Step 6. Thus, the stability of the algorithm is determined by (38) and (40) alone. Solutions of these two equations have the form $a_v^n = A^n a_v^0$ and $v_b^n = A^n v_b^0$, where the amplification factor, A, solves the quadratic

$$M_r^2 A^2 - 2A + 1 = 0,$$

whose roots are given by

$$A = \frac{1}{M_r^2}\left[1 \pm \sqrt{1 - M_r^2}\,\right].$$

Perturbations to the components of the solution given by the time-stepping described by Algorithm 3 are bounded if $|A| < 1$, and this occurs when $M_r > 1$, i.e. if the mass of the rigid body is larger than the added mass. This result is encapsulated in the following theorem:

Theorem 1. *The traditional-partitioned (TP-RB) algorithm given in Algorithm 3 for the added-mass model problem MP-AM is stable if and only if the mass of the body is greater than the total mass of the fluid*

$$M_r = \frac{m_b}{\rho L H} = \frac{m_b}{M_a} > 1.$$

5.1.3. Analysis of the AMP-RB algorithm for MP-AM

In order to show that the added-mass instability found in the traditional approach is suppressed in the AMP scheme, consider the AMP-RB algorithm outlined in Algorithm 2. For the MP-AM model problem, the fully discretized scheme reduces to the one described in detail in Algorithm 4. In Steps 3 and 6 of Algorithm 4 the calculation of the body acceleration is coupled to the elliptic equation for the fluid pressure through the added-mass interface conditions. These are the key steps which suppress the added-mass instability.

Algorithm 4 AMP-RB scheme for MP-AM
Added-mass model problem in a rectangular geometry.

//Preliminary body evolution step

1. $a_v^{(e)} = 2a_v^n - a_v^{n-1}, \qquad v_b^{(e)} = v_b^{n-1} + 2\Delta t\, a_v^n,$

// Prediction steps

2. $\hat{v}_j^{(p)} = \hat{v}_j^n - \frac{3\Delta t}{2\rho} D_0 \hat{p}_j^n + \frac{\Delta t}{2\rho} D_0 \hat{p}_j^{n-1}, \quad j = 1, 2, \ldots, N-1, \qquad \hat{v}_0^{(p)} = v_b^{(e)}, \quad D_0 \hat{v}_N^{(p)} = 0,$

3. $D_+ D_- \hat{p}_j^{(p)} = 0, \quad j = 1, 2, \ldots, N-1, \qquad \begin{cases} D_{yh}\hat{p}_0^{(p)} + \rho a_v^{(p)} = 0 \\ m_b a_v^{(p)} + L\hat{p}_0^{(p)} = g_v(t^{n+1}) \end{cases}, \quad \hat{p}_N^{(p)} = \hat{p}_H(t^{n+1}),$

4. $v_b^{(p)} = v_b^n + \frac{\Delta t}{2}(a_v^{(p)} + a_v^n),$

// Correction steps

5. $\hat{v}_j^{n+1} = \hat{v}_j^n - \frac{\Delta t}{2\rho}(D_0 \hat{p}_j^{(p)} + D_0 \hat{p}_j^n), \quad j = 1, 2, \ldots, N-1, \qquad \hat{v}_0^{n+1} = v_b^{(p)}, \quad D_0 \hat{v}_N^{n+1} = 0,$

6. $D_+ D_- \hat{p}_j^{n+1} = 0, \quad j = 1, 2, \ldots, N-1, \qquad \begin{cases} D_{yh}\hat{p}_0^{n+1} + \rho a_v^{n+1} = 0 \\ m_b a_v^{n+1} + L\hat{p}_0^{n+1} = g_v(t^{n+1}) \end{cases}, \quad \hat{p}_N^{n+1} = \hat{p}_H(t^{n+1}),$

7. $v_b^{n+1} = v_b^n + \frac{\Delta t}{2}(a_v^{n+1} + a_v^n).$

The first two steps in Algorithm 4 result in preliminary values for the velocity and acceleration of the rigid body as well as a predicted value for the discrete grid function holding the fluid velocity. However, these values are not used in subsequent steps of the algorithm for the MP-AM model problem, and so the first important calculation occurs in Step 3. The solution of the discrete elliptic equation defined at this step is given by

$$\hat{p}_j^{(p)} = \hat{p}(y_j, t^{n+1}), \qquad a_v^{(p)} = a_v(t^{n+1}),$$

where $\hat{p}(y,t)$ and $a_v(t)$ are the exact fluid pressure and vertical body acceleration given in (29) and (32), respectively. The predicted value for the vertical velocity of the rigid body in Step 4 is a trapezoidal rule quadrature of the body accelerations at t^n and t^{n+1}, and this value sets the (spatially uniform) fluid velocity in Step 5 to be

$$\hat{v}_j^{n+1} = v_b^{(p)} = v_b^n + \frac{\Delta t}{2}\big(a_v(t^{n+1}) + a_v(t^n)\big). \tag{41}$$

Step 6 repeats the calculation in Step 3 to give

$$\hat{p}_j^{n+1} = \hat{p}(y_j, t^{n+1}), \qquad a_v^{n+1} = a_v(t^{n+1}), \tag{42}$$

and thus the result of Step 7 is

$$v_b^{n+1} = v_b^n + \frac{\Delta t}{2}\big(a_v(t^{n+1}) + a_v(t^n)\big). \tag{43}$$

Assuming that $m_b + M_a$ is bounded away from zero, the discrete solutions for pressure and acceleration in (42) are readily bounded by the forcing function, $g_v(t) - Lp_H(t)$. Also, since the discrete solutions for the velocities in (41) and (43) are simply trapezoidal rule quadratures of the exact solution, we conclude that the discrete solution of the MP-AM model problem given by the AMP-RB algorithm is unconditionally stable, spatially exact, and second-order accurate in time. This result is encapsulated in the following theorem:

Theorem 2. *The AMP-RB algorithm given in Algorithm 4 for the model problem MP-AM is unconditionally stable provided there exists a constant $K > 0$ such that*

$$m_b + M_a \geq K.$$

Note that this result is valid independent of the optional velocity correction (VC) step of the AMP-RB algorithm which plays no important role for the added-mass case.

5.2. Analysis of a model problem for added damping

We derive a model problem for added-damping and then derive an approximation to the added-damping coefficient (21) by considering the solution to a discrete variational problem. With an approximation of this coefficient in hand, we then perform a stability analysis of the AMP-RB algorithm and compare the results to that for the TP-RB algorithm.

5.2.1. Added-damping model problem MP-AD

The added-damping model is obtained from the $k = 0$ mode in the Fourier expansion of the fluid variables together with the equation for the horizontal component of the rigid body. This results in the MP-AD model given by

$$\text{MP-AD:} \begin{cases} \rho \dfrac{\partial \hat{u}}{\partial t} = \mu \dfrac{\partial^2 \hat{u}}{\partial y^2}, & y \in (0, H), \\ m_b \dfrac{du_b}{dt} = \mu L \dfrac{\partial \hat{u}}{\partial y}(0,t) + g_u(t), & \\ \hat{u}(0,t) = u_b(t), \quad \hat{u}(H,t) = \hat{u}_H(t), & \end{cases} \tag{44}$$

where the subscript on the coefficient function for the horizontal component of the fluid velocity corresponding to $k = 0$ has been dropped for notational convenience.

5.2.2. Derivation of the added-damping coefficient

In order to derive an approximation of the added-damping coefficient (21) which appears in the interface condition (22), consider an implicit (monolithic) discretization of the MP-AD model problem of the form

$$\rho\frac{\hat{u}_j-\hat{u}_j^n}{\Delta t}=\mu\left[\alpha D_+D_-\hat{u}_j+(1-\alpha)D_+D_-\hat{u}_j^n\right],\quad j=1,2,\ldots N-1, \tag{45}$$

$$m_b a_u=\mu L\, D_{yh}\hat{u}_0+g_u(t^{n+1}), \tag{46}$$

$$\hat{u}_0=u_b,\qquad \hat{u}_N=\hat{u}_H(t^{n+1}), \tag{47}$$

where $\hat{u}_j$, u_b and a_u denote discrete approximations at t^{n+1}. It is convenient to introduce the acceleration of the body, a_u, in (46) and relate it to the velocity of the body by

$$\frac{u_b-u_b^n}{\Delta t}=\bar{\alpha}a_u+(1-\bar{\alpha})a_u^n. \tag{48}$$

The divided difference operators, D_+, D_- and D_{yh}, appearing in (45) and (46) are the same as those defined in (33) and (34), although it is informative to also consider a first-order approximation for which $D_{yh}=D_+$. The constants α and $\bar{\alpha}$ are included in (45) and (48) to allow some flexibility in the choice of the time-stepping scheme. Typical choices for the implicit scheme are $\alpha=\bar{\alpha}=1/2$ corresponding to a second-order accurate trapezoidal method and $\alpha=\bar{\alpha}=1$ for a first-order accurate backward Euler method.

We recall that the added-damping coefficient, $\mathcal{D}^u$, is related to the derivative of the integral of the shear stress on the body, $\mathcal{I}_u$, in (19) with respect to the horizontal component of the velocity of the body, u_b. In the context of the discretization of the model problem in (45)–(48), the added-damping coefficient is given by

$$\mathcal{D}^u=-\mu L D_{yh}\hat{w}_0, \tag{49}$$

where

$$\hat{w}_j=\frac{\partial\hat{u}_j}{\partial u_b},\qquad j=0,1,\ldots,N.$$

The grid function $\hat{w}_j$ is obtained from the solution of the discrete variational problem given by

$$\frac{\rho}{\Delta t}\hat{w}_j=\mu\alpha D_+D_-\hat{w}_j,\quad j=1,2,\ldots N-1, \tag{50}$$

$$\hat{w}_0=1,\qquad \hat{w}_N=0, \tag{51}$$

which is derived from (45) and (47) upon differentiation with respect to u_b. The discrete Helmholtz equation in (50) can be written in the form

$$\hat{w}_{j+1}-2\hat{w}_j+\hat{w}_{j-1}=\delta^2\hat{w}_j, \tag{52}$$

where

$$\delta\stackrel{\text{def}}{=}\frac{\Delta y}{\sqrt{\alpha\nu\Delta t}}, \tag{53}$$

is a dimensionless parameter defined by the ratio of the grid spacing in the vertical direction (normal to the interface) and a viscous length $\sqrt{\alpha\nu\Delta t}$ determined by the time step. The solution of the difference equation in (52) with boundary conditions in (51) can be written in the form

$$\hat{w}_j=\frac{\eta^j-\eta^{2N-j}}{1-\eta^{2N}}, \tag{54}$$

where

$$\eta=1+\delta^2/2-\delta\sqrt{1+\delta^2/4}=\frac{1}{1+\delta^2/2+\delta\sqrt{1+\delta^2/4}}<1. \tag{55}$$

The quantity $\mathcal{D}^u$ given by (49) can be obtained using various choices of the divided difference operator

D_{yh} and the solution for $\hat{w}_j$ given in (54). For example, if $D_{yh} = D_+$, then

$$\mathcal{D}_1^u = -\mu L D_+ \hat{w}_0 = \mu L \frac{(1-\eta)}{\Delta y} \frac{(1+\eta^{2N-1})}{(1-\eta^{2N})}. \tag{56}$$

The terms involving η^{2N} arise from the boundary condition at $y = H$, and assuming $\eta^{2N} \ll 1$ is usually a reasonable approximation[9]. Neglecting the terms involving η^{2N} gives the approximation

$$\mathcal{D}_1^u \approx \mu L \frac{1-\eta}{\Delta y}. \tag{57}$$

Similarly if D_{yh} is taken to be the second-order accurate one-sided operator defined in (34) and if terms involving η^{2N} are neglected as before, then

$$\mathcal{D}_2^u \approx \mu L \frac{3 - 4\eta + \eta^2}{2\Delta y}. \tag{58}$$

It is therefore clear that different approximations for D_{yh} lead to different approximations to $\mathcal{D}^u$. In practice it is apparently sufficient to use a simple and low-order approximation to $\mathcal{D}^u$ since the AMP-RB algorithm is designed so that the scheme is second-order accurate for any choice of $\mathcal{D}^u$. To this end we base our added-damping coefficient $\mathcal{D}^u$ on the first-order accurate approximation (57). Furthermore, notice that when the viscous terms are treated implicitly, it is typical for $\delta \leq 1$ since the time-step Δt will normally be chosen to exceed the usual explicit time-step restriction by some factor C_ν larger than one (e.g. 10 or 100). Thus in the typical case

$$\frac{\alpha\nu\Delta t}{\Delta y^2} = \frac{1}{\delta^2} > C_\nu > 1 \implies \delta < \frac{1}{\sqrt{C_\nu}} < 1.$$

Note that for δ small, η is a second-order accurate approximation to $e^{-\delta}$, while for large δ both η and $e^{-\delta}$ decay to zero. As a result, the sensible approximation $\eta \approx e^{-\delta}$ leads to the following definition:

Definition 2. *The approximate added-damping coefficient* $\mathcal{D}_n^u$ *and* added-damping length-scale Δn *are defined by*

$$\mathcal{D}_n^u \stackrel{\text{def}}{=} \mu L \frac{1 - e^{-\delta}}{\Delta y} = \mu L \frac{1}{\Delta n}, \tag{59}$$

$$\Delta n \stackrel{\text{def}}{=} \frac{\Delta y}{1 - e^{-\delta}}. \tag{60}$$

The *added-damping length-scale* Δn is a distance in the normal direction to the boundary with limiting behaviours

$$\Delta n \sim \begin{cases} \sqrt{\alpha\nu\Delta t} & \text{for } \delta \to 0, \\ \Delta y & \text{for } \delta \to \infty. \end{cases}$$

Thus the added-damping length-scale Δn varies in size between the viscous length $\sqrt{\alpha\nu\Delta t}$ and the grid-spacing Δy normal to the boundary as δ varies between zero and infinity. It is important that Δn has approximately the correct behaviour as δ varies since this makes it possible to choose the coefficient of the added-damping once, without requiring it to vary as a function of other problem parameters, see Section 5.2.3.

5.2.3. Analysis of the TP-RB and AMP-RB algorithms for MP-AD

Consider now the stability of the TP-RB and AMP-RB algorithms given in Algorithms 1 and 2, respectively, for the MP-AD model problem. Algorithm 5 gives the specific steps for both algorithms, where the TP-RB scheme is obtained for the choice $\beta_d = 0$ (so that the added-damping term vanishes) and the

[9]The assumption $\eta^{2N} \ll 1$ is usually reasonable unless the fluid layer is very thin, i.e. of the size of the viscous length $\sqrt{\alpha\nu\Delta t}$, or N is small. When $\eta^{2N} \ll 1$ is not a good approximation, equation (56) indicates that a larger value for the added-damping coefficient would result.

AMP-RB scheme corresponds to the choice $\beta_d > 0$. The added-damping coefficient $\mathcal{D}_n^u$ appearing in Step 3 of the algorithm is defined in (59). The horizontal component of the fluid velocity satisfies a discrete diffusion equation in Steps 2 and 5 of the algorithm (and optionally in Step 8). For convenience the boundary at $y = H$ is taken to be at infinity where the solution is assumed to be bounded. This choice is made to simplify the algebraic details of the analysis somewhat, but it has little effect on the main results assuming H is not small in relation to the grid spacing Δy. As before, we consider the homogeneous case with $g_u(t)$ set to zero, and regard the discrete variables as perturbations to the exact solution of the discrete equations. The stability analysis considers the growth or decay of these perturbations. We proceed with the analysis by first assuming that $\beta_d > 0$, and then consider the limiting case $\beta_d = 0$ in the end.

Algorithm 5 TP-RB scheme ($\beta_d = 0$) and AMP-RB scheme ($\beta_d > 0$) for MP-AD
Added-damping model problem in a rectangular geometry.

// Preliminary body evolution step

1. $a_u^{(e)} = 2a_u^n - a_u^{n-1}, \qquad u_b^{(e)} = u_b^{n-1} + 2\Delta t\, a_u^n,$

// Prediction steps

2. $\hat{u}_j^{(p)} = \hat{u}_j^n + \frac{\nu\Delta t}{2}\big(D_+D_-\hat{u}_j^{(p)} + D_+D_-\hat{u}_j^n\big), \quad j = 1, 2, \ldots, \qquad \hat{u}_0^{(p)} = u_b^{(e)}, \quad \lim_{j\to\infty} |\hat{u}_j^{(p)}| < \infty,$
3. $(m_b + \beta_d\Delta t\mathcal{D}_n^u)a_u^{(p)} = \mu L\big(D_{yh}\hat{u}_0^{(p)}\big) + \beta_d\Delta t\mathcal{D}_n^u a_u^{(e)} + g_u(t^{n+1}),$
4. $u_b^{(p)} = u_b^n + \frac{\Delta t}{2}(a_u^{(p)} + a_u^n),$

// Correction steps

5. $\hat{u}_j^{n+1} = \hat{u}_j^n + \frac{\nu\Delta t}{2}\big(D_+D_-\hat{u}_j^{n+1} + D_+D_-\hat{u}_j^n\big), \quad j = 1, 2, \ldots, \qquad \hat{u}_0^{n+1} = u_b^{(p)}, \quad \lim_{j\to\infty} |\hat{u}_j^{n+1}| < \infty,$
6. $(m_b + \beta_d\Delta t\mathcal{D}_n^u)a_u^{n+1} = \mu L\big(D_{yh}\hat{u}_0^{n+1}\big) + \beta_d\Delta t\mathcal{D}_n^u\, a_u^{(p)} + g_u(t^{n+1}),$
7. $u_b^{n+1} = u_b^n + \frac{\Delta t}{2}(a_u^{n+1} + a_u^n),$

// Fluid-velocity correction step (optional)

8. $\hat{u}_j^{n+1} = \hat{u}_j^n + \frac{\nu\Delta t}{2}\big(D_+D_-\hat{u}_j^{n+1} + D_+D_-\hat{u}_j^n\big), \quad j = 1, 2, \ldots, \qquad \hat{u}_0^{n+1} = u_b^{n+1}, \quad \lim_{j\to\infty} |\hat{u}_j^{n+1}| < \infty,$

To address the stability of the schemes we proceed along the classical lines of GKS stability theory [37]. As such, consider solutions to the homogeneous equations of the form

$$\hat{u}_j^n = A^n\,\hat{u}_j^0, \qquad u_b^n = A^n\,u_b^0, \qquad a_u^n = A^n\,a_u^0, \tag{61}$$

where A is an amplification factor. It is also convenient to define

$$\hat{u}_j^{(p)} = A^{n+1}\bar{u}_j^{(p)}, \qquad u_b^{(k)} = A^{n+1}\bar{u}_b^{(k)}, \qquad a_u^{(k)} = A^{n+1}\bar{a}_u^{(k)}, \qquad k = e \text{ or } p, \tag{62}$$

for the intermediate values in Algorithm 5. We now seek solutions of the equations with $|A| > 1$ so that if no solutions of this form can be found, then the time-stepping scheme is stable. Substitution of (61) and (62) into Step 5 yields the following difference equation

$$A\hat{u}_j^0 = \hat{u}_j^0 + \frac{\nu\Delta t}{2}(A+1)D_+D_-\hat{u}_j^0, \quad j = 1, 2, \ldots, \qquad \hat{u}_0^0 = \bar{u}_b^{(p)}, \quad \lim_{j\to\infty} |\hat{u}_j^0| < \infty, \tag{63}$$

with solutions of the form $\hat{u}_j^0 = K\,\xi^j$, where ξ is a complex constant. Using the assumption that $|A| > 1$ and the boundary conditions gives

$$\hat{u}_j^0 = \bar{u}_b^{(p)}\xi^j, \tag{64}$$

where $|\xi| < 1$ is given by

$$\xi = q - \sqrt{q^2 - 1}, \qquad q = 1 + \frac{\delta^2}{2}\left(\frac{A-1}{A+1}\right), \tag{65}$$

with δ defined in (53) for $\alpha = 1/2$. Similarly, substitution of (61) and (62) into Step 2 yields the difference equation

$$A\left(1 - \frac{\nu\Delta t}{2}D_+D_-\right)\bar{u}_j^{(p)} = \left(1 + \frac{\nu\Delta t}{2}D_+D_-\right)\hat{u}_j^0, \quad j = 1, 2, \ldots, \qquad \bar{u}_0^{(p)} = \bar{u}_b^{(e)}, \quad \lim_{j\to\infty}|\bar{u}_j^{(p)}| < \infty, \tag{66}$$

with $\hat{u}_j^0$ given in (64). The solution of (66) has the form

$$\bar{u}_j^{(p)} = \left(\bar{u}_b^{(e)} - \bar{u}_b^{(p)}\right)\eta^j + \hat{u}_j^0, \tag{67}$$

where η is defined as before in (55).

The solutions for $\hat{u}_j^0$ in (64) and $\bar{u}_j^{(p)}$ in (67) are inserted into Steps 3 and 6 of Algorithm 5 to eliminate the fluid velocities in favor of the velocities of the body. The remaining steps of the algorithm are then given in terms of velocities and accelerations of the body alone. For example, the equations in Steps 6 and 7 with the forms in (61) and (62), and using the solution in (64), can be written as the following system of equations

$$\begin{bmatrix} 0 & m_b + \beta_d\Delta t\mathcal{D}_n^u \\ A-1 & -\frac{\Delta t}{2}(A+1) \end{bmatrix}\begin{bmatrix} u_b^0 \\ a_u^0 \end{bmatrix} = \begin{bmatrix} \mu L(D_{yh}\xi^j)\big|_{j=0} & \beta_d\Delta t\mathcal{D}_n^u \\ 0 & 0 \end{bmatrix}\begin{bmatrix} \bar{u}_b^{(p)} \\ \bar{a}_u^{(p)} \end{bmatrix}. \tag{68}$$

A similar analysis of the equations in Steps 3 and 4 gives

$$\begin{aligned} &\begin{bmatrix} \mu L\left[(D_{yh}\eta^j)\big|_{j=0} - (D_{yh}\xi^j)\big|_{j=0}\right] & m_b + \beta_d\Delta t\mathcal{D}_n^u \\ A & -\frac{\Delta t}{2}A \end{bmatrix}\begin{bmatrix} \bar{u}_b^{(p)} \\ \bar{a}_u^{(p)} \end{bmatrix} \\ &\quad = \begin{bmatrix} \mu L(D_{yh}\eta^j)\big|_{j=0} & \beta_d\Delta t\mathcal{D}_n^u \\ 0 & 0 \end{bmatrix}\begin{bmatrix} \bar{u}_b^{(e)} \\ \bar{a}_u^{(e)} \end{bmatrix} + \begin{bmatrix} 0 & 0 \\ 1 & \frac{\Delta t}{2} \end{bmatrix}\begin{bmatrix} \bar{u}_b^0 \\ \bar{a}_u^0 \end{bmatrix}. \end{aligned} \tag{69}$$

Finally, the two equations in Step 1 can be written as the system

$$\begin{bmatrix} \bar{u}_b^{(e)} \\ \bar{a}_u^{(e)} \end{bmatrix} = \frac{1}{A^2}\begin{bmatrix} 1 & 2\Delta t A \\ 0 & 2A-1 \end{bmatrix}\begin{bmatrix} \bar{u}_b^0 \\ \bar{a}_u^0 \end{bmatrix}. \tag{70}$$

The intermediates states, $\left[\bar{u}_b^{(k)}, \bar{a}_u^{(k)}\right]^T$, $k = e$ and p, can be eliminated from the linear systems in (68), (69) and (70) to give a homogeneous system of the form

$$M\begin{bmatrix} \bar{u}_b^0 \\ \bar{a}_u^0 \end{bmatrix} = 0, \tag{71}$$

where the 2×2 matrix M involves the amplification factor A and the various parameters of the problem. Nontrivial solutions of (71) exist if $\det(M) = 0$, which leads to the following theorem:

Theorem 3. *The AMP-RB algorithm without the velocity-correction, Step 8, given in Algorithm 5 for the model problem MP-AD, is stable in the sense of Godunov and Ryabenkii if and only if there are no roots with $|A| > 1$ to the following equation:*

$$\mathcal{N}_b(A) \stackrel{\text{def}}{=} \gamma_b(A-1)^3 + \gamma_0\left[\bar{m}_b(A-1) + C_\xi(A+1)\right]A^2 = 0, \tag{72}$$

where

$$\gamma_b \stackrel{\text{def}}{=} (2\beta_d\bar{\mathcal{D}}^u - C_\xi)(2\beta_d\bar{\mathcal{D}}^u - C_\eta), \qquad \gamma_0 \stackrel{\text{def}}{=} \bar{m}_b + 4\beta_d\bar{\mathcal{D}}^u - C_\eta.$$

Here, $\bar{\mathcal{D}}^u$ and $\bar{m}_b$ are a dimensionless added-damping coefficient and body mass, respectively, given by

$$\bar{\mathcal{D}}^u \stackrel{\text{def}}{=} \frac{\Delta y \mathcal{D}_n^u}{\mu L} = 1 - e^{-\delta}, \tag{73}$$

$$\bar{m}_b \stackrel{\text{def}}{=} \left(\frac{m_b}{\rho L \Delta y}\right)\delta^2, \tag{74}$$

and C_ξ and C_η are dimensionless Dirichlet-to-Neumann transfer coefficients given by

$$C_\xi \stackrel{\text{def}}{=} -\Delta y(D_{yh}\xi^j)\big|_{j=0} = \frac{3 - 4\xi + \xi^2}{2}, \qquad C_\eta \stackrel{\text{def}}{=} -\Delta y(D_{yh}\eta^j)\big|_{j=0} = \frac{3 - 4\eta + \eta^2}{2}, \tag{75}$$

where ξ and η, which depend on A and δ, are defined in (65) and (55), respectively.

A similar stability analysis can be performed for Algorithm 5 with the optional fluid-velocity correction step (Step 8) included. This leads to the following theorem:

Theorem 4. *The AMP-RB algorithm with the velocity-correction, Step 8, given in Algorithm 5 for the model problem MP-AD, is stable in the sense of Godunov and Ryabenkii if and only if there are no roots with $|A| > 1$ to the following equation*

$$\mathcal{N}_v(A) \stackrel{\text{def}}{=} \gamma_v(A-1)^3 + \gamma_0\big[\bar{m}_b(A-1) + C_\xi(A+1)\big]A^2 = 0, \tag{76}$$

where γ_b in (72) is replaced by

$$\gamma_v = (2\beta_d\bar{\mathcal{D}}^u - C_\eta)^2,$$

in (76) while the other terms are unchanged.

Stability regions for Algorithm 5 with, and without, the velocity-correction step, are defined as follows.

Definition 3. *The stability region, $\mathcal{S}_b = \mathcal{S}_b\{\bar{m}_b, \delta, \beta_d\}$, for Algorithm 5 with no velocity-correction is defined to be the set of values for the non-dimensional parameters $\bar{m}_b \geq 0$, $\delta > 0$ and $\beta_d \geq 0$ where there are no roots A with $|A| > 1$ to $\mathcal{N}_b(A) = 0$ given in (72).*

Definition 4. *The stability region, $\mathcal{S}_v = \mathcal{S}_v\{\bar{m}_b, \delta, \beta_d\}$, for Algorithm 5 with velocity-correction is defined to be the set of values for the non-dimensional parameters $\bar{m}_b \geq 0$, $\delta > 0$ and $\beta_d \geq 0$ where there are no roots A with $|A| > 1$ to $\mathcal{N}_v(A) = 0$ given in (76).*

Portions of the stability regions $\mathcal{S}_b$ and $\mathcal{S}_v$ are presented in Figures 4 and 5. Generation of these plots is nontrivial, and so it is appropriate to say a few words about our procedure for doing so. Consider first the computation of $\mathcal{S}_b$ (the computation of $\mathcal{S}_v$ being similar). Note that while $\mathcal{N}_b$ in (72) appears to be a cubic polynomial in A, its coefficients involve square roots of a rational function of A through the transfer coefficients C_ξ and C_η and the definitions of ξ and η. However, manipulation of (72), including squaring both sides of the equation, reveals a polynomial in A of degree eight. Note that not all roots of this eighth-degree polynomial are valid since squaring the equation may introduce spurious roots. Nonetheless, all eight roots of this polynomial can be found numerically, for example by determining the eigenvalues of the corresponding companion matrix, and valid roots can be identified as being those that satisfy the original equation $\mathcal{N}_b = 0$. The scheme is determined to be unstable if any of these valid roots satisfy $|A| > 1$, otherwise it is stable. This procedure can then be carried out with a fine grid of points in the parameter space $(\bar{m}_b, \delta, \beta_d)$ to reveal the stability region.

Alternately, the boundaries separating stable and unstable regions can be sought directly by using the fact that points on this boundary satisfy $|A| = 1$ which suggests the transformation $A = e^{i\theta}$ with $\theta \in \mathbb{R}$. Furthermore, note that the equation $\mathcal{N}_b = 0$ is a quadratic equation in β_d. Given values for θ, $\bar{m}_b$ and δ

one solves this quadratic equation for β_d to give two values $\beta_d = \beta_d^{\pm}(\theta; \bar{m}_b, \delta)$. Values of θ where β_d is real denote points on the stability boundary. These values can be determined as the real roots θ of the scalar equations $\mathcal{B}^{\pm}(\theta) \stackrel{\text{def}}{=} \text{Im}(\beta_d^{\pm}(\theta; \bar{m}_b, \delta)) = 0$. Note that the case $A \to 1$ requires some care and reduces to the condition $\gamma_0 = 0$.

The stability regions $\mathcal{S}_b$ and $\mathcal{S}_v$ depend on the three parameters $(\bar{m}_b, \delta, \beta_d)$ where for clarity we recall the expressions for $\bar{m}_b$ and δ,

$$\bar{m}_b = \frac{m_b}{\rho L \Delta y}\,\delta^2, \quad \delta = \frac{\Delta y}{\sqrt{\nu \Delta t/2}}.$$

For plotting purposes it is convenient to show cuts through the three-dimensional space by plotting two-dimensional contours of the regions by holding one of the three parameters fixed and letting the other two vary. The lower plots in Figures 4 and 5 show such cuts through the stability regions. The lower left plots show the stable and unstable regions for a typical value of $\delta = 0.5$ while the lower right plots show the regions for the difficult case $\bar{m}_b = 0$ when added damping effects are greatest. The stable regions are shown in white, while *instability regions* are shaded in different colors which correspond to unstable modes of different character. Characterization of the various unstable modes is useful since it sheds light on the origin of instabilities that occur in practice (e.g. β_d is taken to be too small). In order to aid in understanding these instabilities, the upper panel of plots in Figures 4 and 5 show the spatial and temporal evolution of the various unstable modes.

Instability region I corresponds to having provided insufficient stabilization of added-damping effects (or none at all in the case of the traditional scheme with $\beta_d = 0$), and occurs for very light or massless bodies (a *light* body being characterized by the non-dimensional body mass $\bar{m}_b$). This mode is characterized by A being real with $A > 1$. The behaviour of the unstable mode in time is A^n, $n = 0, 1, 2, \ldots$ and in space ξ^j, $j = 0, 1, 2, \ldots$. The real parts of these modes are shown at the top of Figures 4 and 5, the $Re(A^n)$ being scaled by its maximum absolute value for graphical purposes. The unstable modes in region I grow monotonically and *exponentially* fast in time, and decay monotonically in space from a maximal value on the boundary $j = 0$.

Instability region II also corresponds to having provided insufficient stabilization of added-damping effects (or none at all in the case of the traditional scheme with $\beta_d = 0$), and exists for slightly larger rigid body masses than those characterized by region I. This mode is characterized by a complex root A, which implies an oscillatory exponential growth in time. The spatial behaviour is that of a rapidly decaying boundary layer with mild oscillations. Note that this root corresponds to a bifurcation of the real root from region I into a complex conjugate pair.

Instability region III occurs only for the scheme without velocity correction and is especially prevalent for small values of δ (i.e. *large* implicit time-step). The instability is characterized by a real root with $A < -1$ corresponding to an exponentially growing plus-minus type mode in time, and an exponentially decaying mode in space.

Instability region IV occurs for the scheme both with and without velocity correction and is associated with having provided excessive stabilization against added-damping effects. This instability is characterized by a complex root for A, that for large values of β_d exhibits rather slow exponential growth in time. This mode can be the most difficult to detect as it may take many time-steps to become dominant.

Figure 4 shows the four instability regions for $\delta = 0.5$. Here we observe that for β_d between 2 and 4, approximately, the AMP-RB-NVC scheme (no velocity correction) is stable for any value of the mass-ratio $\bar{m}_b \geq 0$. The lower-right plot in Figure 4 shows the stable and unstable regions for the limiting case of $\bar{m}_b = 0$, where for small δ the AMP-RB-NVC scheme is unstable except for a very narrow gap near $\beta \approx 0.54$. For practical FSI computations, this sensitivity makes the scheme with no velocity correction unusable for very light bodies.

On the other hand, Figure 5 presents the corresponding plots for the AMP-RB-VC scheme (with velocity correction). The additional velocity-correction step is seen to improve the stability of the scheme, especially for situations when added-damping effects are large. In particular the green instability region II found in $\mathcal{S}_b$ is no longer present in $\mathcal{S}_v$. As a result there is range of β_d centered about $\beta_d = 1$ approximately where the scheme is stable even as $\bar{m}_b \to 0$. This makes the scheme more robust when applied to practical FSI problems. The stability results presented in Figures 4 and 5 are confirmed in the numerical results presented

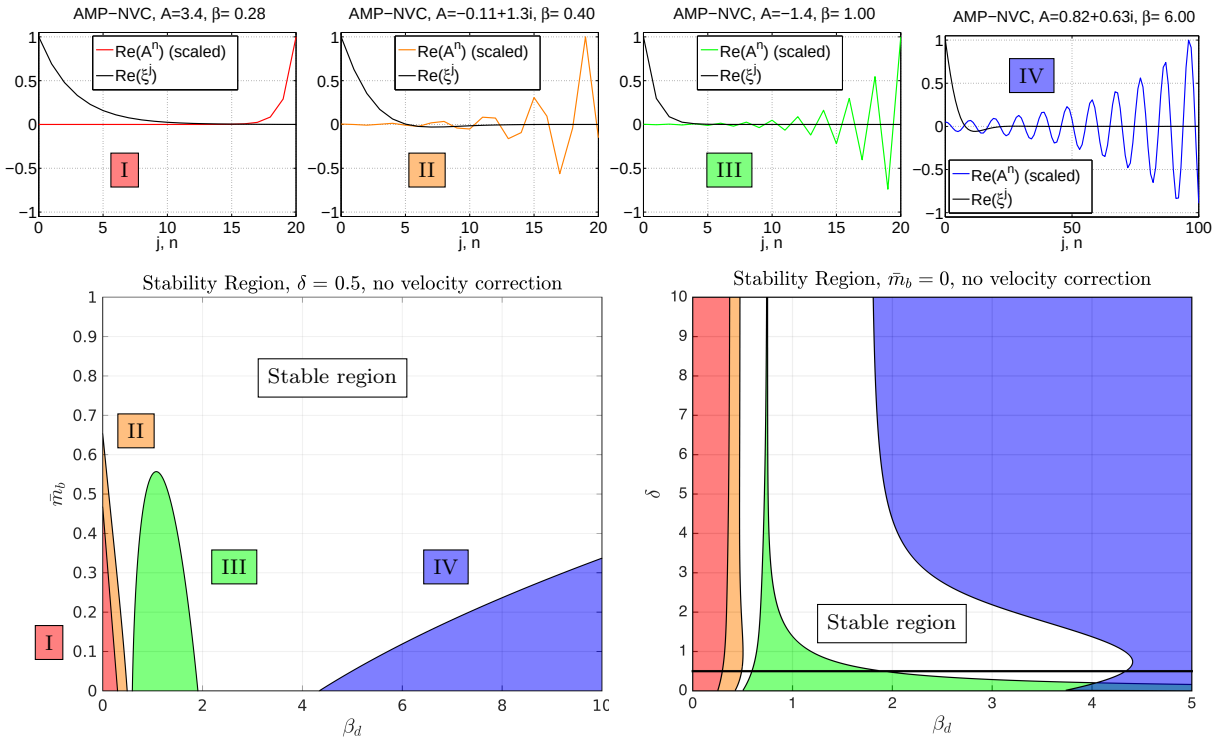

Figure 4: Stability regions and unstable modes for the AMP-RB-scheme with no velocity correction. Bottom left: stability region in the β_d–$\bar{m}_b$ plane for $\delta = .5$; unstable shaded regions are marked according to the form of the instability. Bottom: right: stability region in the β_d–δ plane for the zero-mass body. Top: unstable modes in space and time for the four instability types ($\delta = .5$ and $\bar{m}_b = 0$).

in Section 7, and in the results of Part II.

Finally, consider the traditional-partitioned (TP-RB) scheme for the added-damping model problem corresponding to $\beta_d = 0$ in Algorithm 5 (no velocity correction). The stability region in this case depends on $\bar{m}_b$ and δ only, and the numerically computed stability region is shown in Figure 6 as the unshaded (white) region. The blue curve in the figure is a simple analytical approximation to the stability boundary given by the formula

$$\bar{m}_b = K_{\rm tp}\, C_\eta \tag{77}$$

where C_η is defined in (75) and $K_{\rm tp} \approx 1.405$ is determined by an approximate fit. The analytic form in (77) defines a sufficient (and nearly necessary) condition from which a time-step restriction can be determined. As can be seen in the subsequent theorem, the TP-RB can have a severe time-step restriction as the mass of the body becomes small.

Theorem 5. *The traditional-partitioned scheme for solving the added-damping model problem MP-AD, using Algorithm 5 with $\beta_d = 0$ and no velocity-correction step, is stable when $\bar{m}_b > 0$ for sufficiently small Δt with $\Delta t \to 0$ as $m_b \to 0$. The stability region depends on $\bar{m}_b$ and δ and the numerically computed stability region is shown in Figure 6. Based on the approximate stability boundary (77), a sufficient and nearly necessary condition for stability is that the time-step must satisfy*

$$\Delta t \lesssim \frac{2}{K_{\rm tp}\, C_\eta}\left(\frac{m_b}{\rho L H}\right)\left(\frac{\Delta y}{H}\right)\frac{H^2}{\nu} \quad \Longrightarrow \quad \Delta t \lesssim \begin{cases} \dfrac{2}{K_{\rm tp}^2}\left(\dfrac{m_b}{\rho L H}\right)^2 \dfrac{H^2}{\nu} & \text{for } \delta \ll 1, \\ \dfrac{4}{3K_{\rm tp}}\left(\dfrac{m_b}{\rho L H}\right)\left(\dfrac{\Delta y}{H}\right)\dfrac{H^2}{\nu} & \text{for } \delta \gg 1. \end{cases} \tag{78}$$

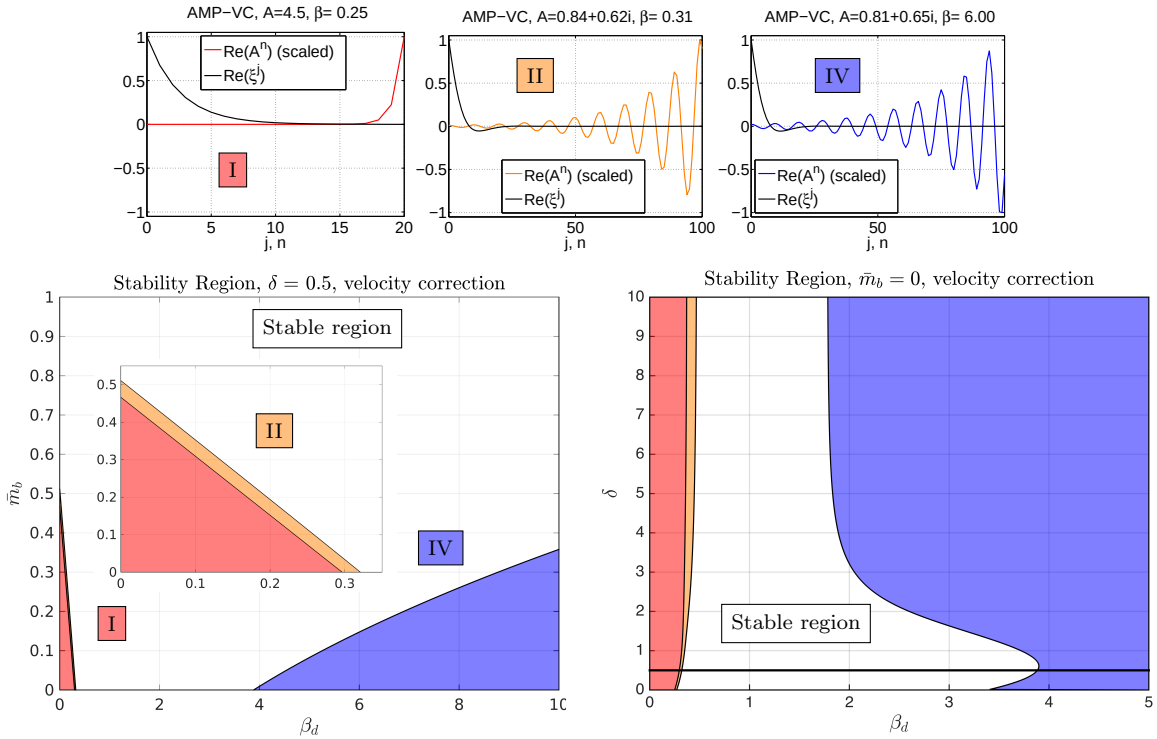

Figure 5: Stability regions and unstable modes for the AMP-RB-scheme with velocity correction. Bottom left: stability region in the β_d–$\bar{m}_b$ plane for $\delta = .5$ with zoom of lower left; shaded unstable regions are marked according to the form of the instability. Bottom: right: stability region in the β_d–δ plane for the zero-mass body. Top: unstable modes in space and time for the three instability types ($\delta = .5$ and $\bar{m}_b = 0$).

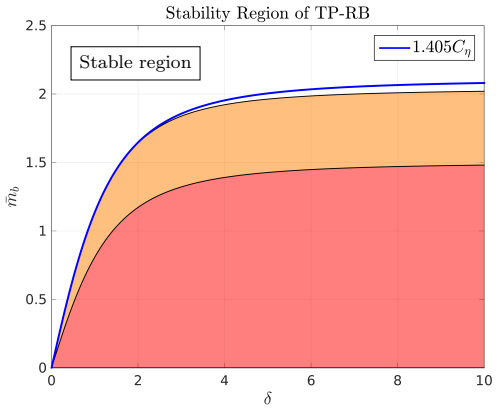

Figure 6: The stability region in the δ–$\bar{m}_b$ plane for the TP-RB scheme for the added-damping model problem. The blue curve is an analytic approximation to the boundary of the stable region.

Equation (78) follows directly from (77) using the definition of $\bar{m}_b$ and the asymptotic forms for C_η given by

$$C_\eta \sim \begin{cases} \delta & \text{for } \delta \ll 1, \\ \frac{3}{2} & \text{for } \delta \gg 1. \end{cases}$$

Thus, although the TP-RB scheme can be stabilized with a sufficiently small value of Δt when the mass of the rigid body is finite, the maximal stable time-step approaches zero as the square of the mass tends to zero, making the TP-RB scheme rapidly impractical for light bodies.

The results of the stability analysis can be confirmed numerically by solving the model problem and

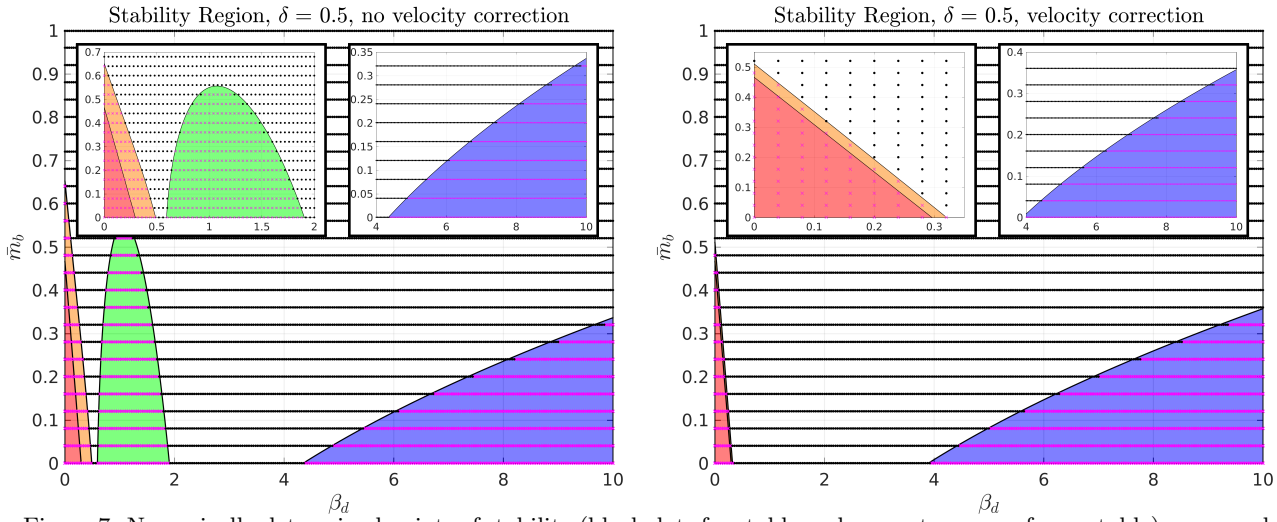

Figure 7: Numerically determined points of stability (black dots for stable and magenta crosses for unstable) compared to the theoretical stability region for the added-damping model problem in a rectangular geometry. Left: the AMP-RB-NVC scheme. Right: the AMP-RB-VC scheme.

checking whether the computed solutions appear to be stable or unstable. Figure 7 shows values of the parameters $(\beta_d, \bar{m}_b)$ with $\delta = 0.5$ held fixed where the AMP-RB scheme, with and without velocity correction, is determined to be stable or unstable. Solutions are computed using the grid $\mathcal{G}^{(4)}$, as defined in Section 7.2, with $\Delta t = 0.05$. The black dots in the figure indicate points where the numerical solution appears to be stable up to a final time of $t = 50$, while the magenta crosses denote points where the solution is unstable. The numerically computed stability region is seen to be in excellent agreement with the theory. There are minor discrepancies near the boundaries of the stability regions but these can be attributed to the final time not being large enough to show the slow unstable growth that would be expected near the stability boundaries.

6. Analysis of FSI model problems in an annular geometry

In this section, we extend the analysis of the AMP-RB algorithm to two FSI model problems in an annular geometry, one focusing on added-mass effects and the other on added-damping. The analysis for the annular geometry, shown in Figure 8, confirms the essential conclusions derived from the simplified rectangular-geometry model problems, including the formulation of the added-damping coefficient $\mathcal{D}^u$ and the determination of the added-damping parameter β_d. For the present problem, the incompressible fluid occupies the annular domain Ω between an inner radius r_1 and an outer radius r_2, and surrounds the rigid body with mass m_b and moment of inertial I_b in the domain Ω_b. As before, we consider small displacements of the rigid body and linearize the motion of the interface separating the fluid and the body about the fixed circle with radius r_1, denoted by Γ_b in the figure.

It is convenient to describe the velocity of the fluid in terms of its components in the radial and circumferential directions, denoted by $u(r, \theta, t)$ and $v(r, \theta, t)$, respectively, where $\mathbf{x} = (r, \theta)$ are polar coordinates, and the fluid pressure is given by $p(r, \theta, t)$. It is sufficient for the purposes of the analysis to consider rotational motion of the body with angular velocity $\omega_b(t)$ and translational motion of the body only in the horizontal

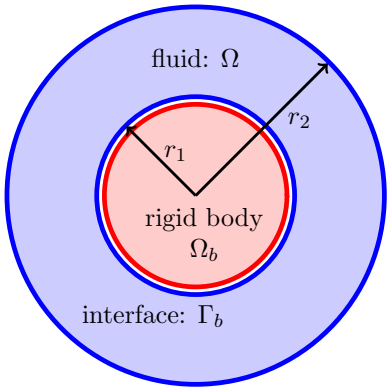

Figure 8: The geometry for the annular geometry FSI model problems.

direction with velocity $u_b(t)$, for example. Under these assumptions, the governing equations are

$$\text{Fluid:} \quad \rho\frac{\partial u}{\partial t} + \frac{\partial p}{\partial r} = \mu\left[\frac{1}{r}\frac{\partial}{\partial r}\left(r\frac{\partial u}{\partial r}\right) + \frac{1}{r^2}\frac{\partial^2 u}{\partial \theta^2} - \frac{u}{r^2} - \frac{2}{r^2}\frac{\partial v}{\partial \theta}\right], \qquad \mathbf{x}\in\Omega, \tag{79}$$

$$\rho\frac{\partial v}{\partial t} + \frac{1}{r}\frac{\partial p}{\partial \theta} = \mu\left[\frac{1}{r}\frac{\partial}{\partial r}\left(r\frac{\partial v}{\partial r}\right) + \frac{1}{r^2}\frac{\partial^2 v}{\partial \theta^2} - \frac{v}{r^2} + \frac{2}{r^2}\frac{\partial u}{\partial \theta}\right], \qquad \mathbf{x}\in\Omega, \tag{80}$$

$$\frac{\partial}{\partial r}(ru) + \frac{\partial v}{\partial \theta} = 0, \qquad \mathbf{x}\in\Omega, \tag{81}$$

$$\text{Rigid body:} \quad m_b\frac{du_b}{dt} = \int_{\Gamma_b}\left(\mathbf{e}_x^T\boldsymbol{\sigma}\mathbf{n}\right)ds + g_u(t), \tag{82}$$

$$I_b\frac{d\omega_b}{dt} = \int_{\Gamma_b} r_1\left(\mathbf{t}^T\boldsymbol{\sigma}\mathbf{n}\right)ds + g_\omega(t), \tag{83}$$

$$\text{Interface:} \quad u = u_b\cos\theta, \qquad v = -u_b\sin\theta + r_1\omega_b, \qquad \mathbf{x}\in\Gamma_b, \tag{84}$$

$$\text{Fluid BCs:} \quad \mathbf{v}(r_2,\theta,t) = 0, \qquad \theta\in[-\pi,\pi]. \tag{85}$$

Here, $\boldsymbol{\sigma}$ is the fluid stress tensor, $\mathbf{n}$ and $\mathbf{t}$ are the unit normal and tangent vectors on Γ_b, respectively, $\mathbf{e}_x$ is the unit normal in the positive x-direction, and $g_u(t)$ and $g_\omega(t)$ are an applied force and torque on the body, respectively. As before, we note that an elliptic equation can be obtained for the fluid pressure using the continuity equation in (81) to eliminate the components of velocity in the momentum equations in (79) and (80). For this annular geometry, the pressure equation is

$$\frac{\partial}{\partial r}\left(r\frac{\partial p}{\partial r}\right) + \frac{1}{r}\frac{\partial^2 p}{\partial \theta^2} = 0, \tag{86}$$

which, along with appropriate boundary conditions, determines the pressure in the fractional-step method used to solve the two model problems described below.

6.1. Model problem MP-AMA for added-mass in an annular geometry

A model problem for added mass can be obtained from the governing equations in (79)–(85) by considering a Fourier-mode decomposition of the fluid variables in the θ-direction. Setting

$$u(r,\theta,t) = \hat{u}(r,t)\cos\theta, \qquad v(r,\theta,t) = -\hat{v}(r,t)\sin\theta, \qquad p(r,\theta,t) = \hat{p}(r,t)\cos\theta, \tag{87}$$

and dropping the decoupled rotational motion of the body gives the MP-AMA model problem of the form

$$\text{MP-AMA:}\quad \begin{cases} \rho\dfrac{\partial \hat{u}}{\partial t} + \dfrac{\partial \hat{p}}{\partial r} = 0, & r \in (r_1, r_2), \\ \rho\dfrac{\partial \hat{v}}{\partial t} + \dfrac{\hat{p}}{r} = 0, & r \in (r_1, r_2), \\ \dfrac{\partial}{\partial r}(r\hat{u}) - \hat{v} = 0, & r \in (r_1, r_2), \\ m_b \dfrac{du_b}{dt} = -r_1 \pi\, \hat{p}(r_1, t) + g_u(t), \\ \hat{u}(r_1, t) = u_b, \\ \hat{u}(r_2, t) = 0. \end{cases} \tag{88}$$

Here the viscous terms have been dropped since it was shown in [23] that the added-mass for a cylindrical rigid body immersed in an incompressible fluid does not depend on viscosity. As a consequence, the boundary condition for the circumferential component of the fluid velocity at $r = r_1$ and r_2 have been dropped as well. The exact solution of the MP-AMA model problem is given by

$$u_b(t) = \frac{1}{m_b + \mathcal{M}_a} \int_0^t g_u(\tau)\, d\tau + u_b(0), \tag{89}$$

$$\hat{p}(r, t) = \frac{\rho r_1 a_u(t)}{r_2/r_1 - r_1/r_2} \left(\frac{r}{r_2} + \frac{r_2}{r} \right), \tag{90}$$

$$\hat{u}(r, t) = \frac{r_2^2 - r^2}{r_2^2 - r_1^2} \left(\frac{r_1}{r} \right)^2 u_b(t), \tag{91}$$

$$\hat{v}(r, t) = \frac{r_2^2 + r^2}{r_2^2 - r_1^2} \left(\frac{r_1}{r} \right)^2 u_b(t), \tag{92}$$

where

$$\mathcal{M}_a = \rho \pi r_1^2 \left[\frac{1 + \left(r_1/r_2\right)^2}{1 - \left(r_1/r_2\right)^2} \right], \tag{93}$$

is the added-mass for this model problem, and the acceleration of the rigid body is given by

$$a_u(t) = \frac{du_b}{dt} = \frac{g_u(t)}{m_b + \mathcal{M}_a}. \tag{94}$$

Note that the added mass $\mathcal{M}_a$ approaches the mass of fluid displaced by the rigid body as r_1/r_2 tends to zero, and that the added mass becomes large as the fluid gap become small (i.e. as $r_1/r_2 \to 1$). The added-mass approaches infinity as the gap narrows since the radial component of the velocity is given as a boundary condition at $r = r_2$ and thus the total volume of fluid is conserved. In the prior MP-AM rectangular geometry case, the corresponding boundary condition was on the pressure, which allowed flow through the boundary. In fact, if the far boundary in MP-AM was taken as a given velocity, then the added-mass would be infinite and the traditional scheme would be unconditionally unstable regardless of the rigid-body mass.

The stability of the AMP-RB algorithm for the MP-AMA model problem is addressed by considering the semi-discrete time-stepping scheme given in Algorithm 6. Here, we have discretized in time which retains the essential features of the AMP-RB algorithm, while the fluid variables remain continuous in space for convenience in the analysis. The superscripts attached to the variables in the algorithm indicate the time level, e.g. $\hat{u}^n \approx \hat{u}(r, t^n)$, and whether the variables are extrapolated or predicted (following the notation used in previous algorithms).

The preliminary values for the velocity and acceleration of the body obtained in Step 1 of Algorithm 6 and the predicted values for the components of the fluid velocity computed in Step 2 are not needed in subsequent steps of the algorithm, and so we begin with the elliptic problem in Step 3, whose solution is given by

$$\hat{p}^{(p)}(r) = \hat{p}(r, t^{n+1}), \qquad a_u^{(p)} = a_u(t^{n+1}),$$

Algorithm 6 AMP-RB scheme for MP-AMA
Added-mass model problem in an annular geometry.

// Preliminary body evolution step

1. $a_u^{(e)} = 2a_u^n - a_u^{n-1}, \qquad u_b^{(e)} = u_b^{n-1} + 2\Delta t\, a_u^n,$

// Prediction steps

2. $\begin{cases} \hat{u}^{(p)} = \hat{u}^n - \frac{3\Delta t}{2\rho}\partial_r \hat{p}^n + \frac{\Delta t}{2\rho}\partial_r \hat{p}^{n-1}, \\ \hat{v}^{(p)} = \hat{v}^n - \frac{3\Delta t}{2\rho r}\hat{p}^n + \frac{\Delta t}{2\rho r}\hat{p}^{n-1}, \end{cases} \quad r \in (r_1, r_2), \qquad \hat{u}^{(p)}(r_1) = u_b^{(e)}, \quad \hat{u}^{(p)}(r_2) = 0,$

3. $\partial_r\big(r\partial_r \hat{p}^{(p)}\big) - \hat{p}^{(p)}/r = 0, \quad r \in (r_1, r_2), \qquad \begin{cases} \partial_r \hat{p}^{(p)}(r_1) + \rho a_u^{(p)} = 0 \\ m_b a_u^{(p)} + \pi r_1 \hat{p}^{(p)}(r_1) = g_u(t^{n+1}) \end{cases}, \quad \partial_r \hat{p}^{(p)}(r_2) = 0,$

4. $u_b^{(p)} = u_b^n + \frac{\Delta t}{2}(a_u^{(p)} + a_u^n),$

// Correction steps

5. $\begin{cases} \hat{u}^{n+1} = \hat{u}^n - \frac{\Delta t}{2\rho}\big(\partial_r \hat{p}^{(p)} + \partial_r \hat{p}^n\big), \\ \hat{v}^{n+1} = \hat{v}^n - \frac{\Delta t}{2\rho r}\big(\hat{p}^{(p)} + \hat{p}^n\big), \end{cases} \quad r \in (r_1, r_2), \qquad \hat{u}^{n+1}(r_1) = u_b^{(p)}, \quad \hat{u}^{n+1}(r_2) = 0,$

6. $\partial_r\big(r\partial_r \hat{p}^{n+1}\big) - \hat{p}^{n+1}/r = 0, \quad r \in (r_1, r_2), \qquad \begin{cases} \partial_r \hat{p}^{n+1}(r_1) + \rho a_u^{n+1} = 0 \\ m_b a_u^{n+1} + \pi r_1 \hat{p}^{n+1}(r_1) = g_u(t^{n+1}) \end{cases}, \quad \partial_r \hat{p}^{n+1}(r_2) = 0,$

7. $u_b^{n+1} = u_b^n + \frac{\Delta t}{2}(a_u^{n+1} + a_u^n).$

where $\hat{p}(r,t)$ and $a_u(t)$ are the exact pressure and acceleration of the body given in (90) and (94), respectively. The updates of the velocity of the body in Step 4 and the components of the fluid velocity in Step 5 use trapezoidal-rule quadratures of the exact body acceleration and fluid pressure which implies these values are unconditionally stable. The elliptic problem for the fluid pressure and the acceleration of the body appears again in Step 6, and the solutions for $\hat{p}^{n+1}(r)$ and a_u^{n+1} agree with the exact solutions at $t = t^{n+1}$ as before. The final step in Algorithm 6 is simply a trapezoidal-rule update of the velocity of the body using the exact body acceleration. Thus provided $m_b + \mathcal{M}_a$ is bounded away from zero, the discrete solution can be bounded in terms of the data which leads to the following result:

Theorem 6. *The AMP-RB algorithm given in Algorithm 6 for the model problem MP-AMA is unconditionally stable provided there exists a constant $K > 0$ such that*

$$m_b + \mathcal{M}_a \geq K.$$

The analysis of the traditional-partitioned scheme for the added-mass model problem MP-AMA closely follows the previous analysis for the rectangular geometry and we simply state the primary result without proof.

Theorem 7. *The traditional-partitioned (TP-RB) algorithm for the added-mass model problem MP-AMA is stable if and only if the mass of the body is greater than the added-mass $\mathcal{M}_a$,*

$$\frac{m_b}{\mathcal{M}_a} > 1.$$

6.2. Model problem MP-ADA for added-damping in an annular geometry

A model problem suitable to study added-damping for the annular geometry can be extracted from the set of equations in (79)–(85) by considering the zeroth Fourier mode of the fluid variables, which is independent of θ. In this model, the circumferential component of the fluid velocity is coupled to the rotation of the rigid body due to the shear stress acting uniformly along the interface Γ_b. The radial component of the

fluid velocity and the fluid pressure decouple and are therefore dropped from the system. The result is the MP-ADA model problem for added damping given by

$$\text{MP-ADA:} \quad \begin{cases} \dfrac{\partial \hat{v}}{\partial t} = \nu \mathcal{L}\hat{v}, & r \in (r_1, r_2), \\ I_b \dfrac{d\omega_b}{dt} = 2\pi r_1^2 \mu \left[r \dfrac{\partial}{\partial r}\left(\dfrac{\hat{v}}{r}\right)\right]_{r=r_1} + g_\omega(t), & \\ \hat{v}(r_1, t) = r_1 \omega_b, & \\ \hat{v}(r_2, t) = 0, & \end{cases} \tag{95}$$

where

$$\mathcal{L}\hat{v} = \frac{1}{r}\frac{\partial}{\partial r}\left(r\frac{\partial \hat{v}}{\partial r}\right) - \frac{\hat{v}}{r^2}.$$

As in the previous model problem for the added-mass, we consider the semi-discrete time-stepping scheme given in Algorithm 7 for the MP-ADA problem. This algorithm uses the angular component of the acceleration of the rigid body, which is denoted $b_\omega^n \approx b_w(t^n)$. The added-damping coefficient, $\mathcal{D}^\omega$, for the annular geometry takes the form

$$\mathcal{D}^\omega = \mu(2\pi r_1) r_1^2 \, \frac{1 - e^{-\tilde{\delta}}}{\Delta r}, \qquad \tilde{\delta} \stackrel{\text{def}}{=} \frac{\Delta r}{\sqrt{\nu \Delta t/2}},$$

which is derived following an analysis of a variational problem similar to that discussed in Section 5.2.2 for the rectangular geometry. To assess the stability of the algorithm, it is important to include a choice for the discrete derivative in the AMP interface condition used in Steps 3 and 6. In the analysis to follow, we use the one-sided difference operator, D_{rh}, analogous to (34), defined by

$$D_{rh} f(r) = \frac{-3f(r) + 4f(r + \Delta r) - f(r + 2\Delta r)}{2\Delta r},$$

where $f(r)$ is a generic function of r.

The stability analysis of the time-stepping scheme for the MP-ADA model problem follows a similar approach to that discussed previously in Section 5.2.3. Therefore, the discussion here is brief and attention is given primarily to the elements of the analysis that are new. We consider the homogeneous problem and set $g_\omega(t) = 0$, $\hat{v}^n = A^n \hat{v}^0$, $\omega_b^n = A^n \omega_b^0$ and $b_\omega^n = A^n b_\omega^0$, where A is an amplification factor. Furthermore, assign $\hat{v}^{(p)} = A^{n+1}\bar{v}^{(p)}$, etc., similar to the definitions in (61) and (62). The solutions of the boundary-value problems in Steps 2 and 5 take the form

$$\bar{v}^{(p)}(r) = r_1\big(\bar{\omega}_b^{(e)} - \bar{\omega}_b^{(p)}\big)\phi_1(r) + \bar{v}^0(r), \qquad \bar{v}^0(r) = r_1 \bar{\omega}_b^{(p)} \phi_2(r), \tag{96}$$

where

$$\phi_m(r) = \frac{I_1(\zeta_m r)K_1(\zeta_m r_2) - I_1(\zeta_m r_2)K_1(\zeta_m r)}{I_1(\zeta_m r_1)K_1(\zeta_m r_2) - I_1(\zeta_m r_2)K_1(\zeta_m r_1)}, \qquad m = 1 \text{ or } 2,$$

and

$$\zeta_1 = \sqrt{\frac{2}{\nu \Delta t}}, \qquad \zeta_2 = \zeta_1 \sqrt{\frac{A-1}{A+1}}.$$

Here, $I_1(z)$ and $K_1(z)$ are modified Bessel functions of the first and second kind of order one. The solutions for $\bar{v}^0(r)$ and $\bar{v}^{(p)}(r)$ in (96) are analogous to the discrete solutions in (64) and (67) found previously.

The solutions for $\bar{v}^0(r)$ and $\bar{v}^{(p)}(r)$ may now be used in the AMP interface conditions in Steps 3 and 6 to eliminate the circumferential velocities of the fluid so that the remaining steps of the algorithm involve the angular velocities and accelerations of the body alone. The analysis of the these remaining steps leads

Algorithm 7 TP-RB scheme ($\beta_d = 0$) and AMP-RB scheme ($\beta_d > 0$) for MP-ADA
Added-damping model problem in an annular geometry.

// Preliminary body evolution step

1. $b_\omega^{(e)} = 2b_\omega^n - b_\omega^{n-1}, \qquad \omega_b^{(e)} = \omega_b^{n-1} + 2\Delta t\, b_\omega^n,$

// Prediction steps

2. $\hat{v}^{(p)} = \hat{v}^n + \frac{\nu\Delta t}{2}\big(\mathcal{L}\hat{v}^{(p)} + \mathcal{L}\hat{v}^n\big), \quad r \in (r_1, r_2) \qquad \hat{v}^{(p)}(r_1) = r_1\omega_b^{(e)}, \quad \hat{v}^{(p)}(r_2) = 0,$
3. $(I_b + \beta_d\Delta t\,\mathcal{D}^\omega)b_\omega^{(p)} = 2\pi r_1^2\mu\big[rD_{rh}(\hat{v}^{(p)}/r)\big]_{r=r_1} + \beta_d\Delta t\,\mathcal{D}^\omega b_\omega^{(e)} + g_\omega(t^{n+1}),$
4. $\omega_b^{(p)} = \omega_b^n + \frac{\Delta t}{2}(b_\omega^{(p)} + b_\omega^n),$

// Correction steps

5. $\hat{v}^{n+1} = \hat{v}^n + \frac{\nu\Delta t}{2}\big(\mathcal{L}\hat{v}^{n+1} + \mathcal{L}\hat{v}^n\big), \quad r \in (r_1, r_2) \qquad \hat{v}^{n+1}(r_1) = r_1\omega_b^{(p)}, \quad \hat{v}^{n+1}(r_2) = 0,$
6. $(I_b + \beta_d\Delta t\,\mathcal{D}^\omega)b_\omega^{n+1} = 2\pi r_1^2\mu\big[rD_{rh}(\hat{v}^{n+1}/r)\big]_{r=r_1} + \beta_d\Delta t\,\mathcal{D}^\omega b_\omega^{(p)} + g_\omega(t^{n+1}),$
7. $\omega_b^{n+1} = \omega_b^n + \frac{\Delta t}{2}(b_\omega^{n+1} + b_\omega^n),$

// Fluid-velocity correction step (optional)

8. $\hat{v}^{n+1} = \hat{v}^n + \frac{\nu\Delta t}{2}\big(\mathcal{L}\hat{v}^{n+1} + \mathcal{L}\hat{v}^n\big), \quad r \in (r_1, r_2) \qquad \hat{v}^{n+1}(r_1) = r_1\omega_b^{n+1}, \quad \hat{v}^{n+1}(r_2) = 0,$

to linear systems analogous to those in (68), (69) and (70), and then to a homogeneous system of the form

$$\widetilde{M}\begin{bmatrix} \bar{\omega}_b^0 \\ \bar{b}_\omega^0 \end{bmatrix} = 0. \tag{97}$$

Nontrivial solutions of (97) are obtained if the determinant of the 2×2 matrix $\widetilde{M}$ is zero which leads to the following theorem.

Theorem 8. *The AMP-RB algorithm without the velocity-correction Step 8, given in Algorithm 7 for the model problem MP-ADA, is stable in the sense of Godunov and Ryabenkii if and only if there are no roots with $|A| > 1$ to the following equation*

$$\widetilde{\mathcal{N}}_b \stackrel{\text{def}}{=} \tilde{\gamma}_b(A-1)^3 + \tilde{\gamma}_0\big[\bar{I}_b(A-1) + \tilde{C}_2(A+1)\big]A^2 = 0, \tag{98}$$

which is similar to the constraint in (72) derived for the MP-AD model problem. The coefficients in (98) are given by

$$\tilde{\gamma}_b \stackrel{\text{def}}{=} (2\beta_d\bar{\mathcal{D}}^\omega - \tilde{C}_2)(2\beta_d\bar{\mathcal{D}}^\omega - \tilde{C}_1), \qquad \tilde{\gamma}_0 \stackrel{\text{def}}{=} \bar{I}_b + 4\beta_d\bar{\mathcal{D}}^\omega - \tilde{C}_1,$$

where $\bar{\mathcal{D}}^\omega$ and $\bar{I}_b$ are a dimensionless added-damping coefficient and moment of inertia of the body, respectively, given by

$$\bar{\mathcal{D}}^\omega \stackrel{\text{def}}{=} \frac{\Delta r\mathcal{D}^\omega}{\mu(2\pi r_1)r_1^2} = 1 - e^{-\tilde{\delta}},$$
$$\bar{I}_b \stackrel{\text{def}}{=} \frac{I_b}{\rho(2\pi r_1)\Delta r\, r_1^2}\,\frac{\tilde{\delta}^2}{2},$$

and $\tilde{C}_1$ and $\tilde{C}_2$ are dimensionless Dirichlet-to-Neumann transfer coefficients given by

$$\tilde{C}_m \stackrel{\text{def}}{=} -\Delta r \left[r D_{rh} \left(\frac{\phi_m(r)}{r} \right) \right]_{r=r_1} = \frac{r_1}{2} \left(\frac{3\phi_m(r_1)}{r_1} - \frac{4\phi_m(r_1+\Delta r)}{r_1+\Delta r} + \frac{\phi_m(r_1+2\Delta r)}{r_1+2\Delta r} \right), \quad m = 1 \text{ or } 2.$$

The constraint equation for A in (98) applies for Algorithm 7 without the optional fluid-velocity correction step. However, as observed in Section 5.2.3 for the MP-AD model problem, including this step improves the stability of the AMP algorithm and then the amplification factor is determined by the following.

Theorem 9. *The AMP-RB algorithm including the velocity-correction Step 8, given in Algorithm 7 for the model problem MP-ADA, is stable in the sense of Godunov and Ryabenkii if and only if there are no roots with $|A| > 1$ to the following equation*

$$\tilde{\mathcal{N}}_v \stackrel{\text{def}}{=} \tilde{\gamma}_v (A-1)^3 + \tilde{\gamma}_0 \left[\bar{I}_b (A-1) + \tilde{C}_2 (A+1) \right] A^2 = 0, \tag{99}$$

where $\tilde{\gamma}_b$ in (98) is replaced by

$$\tilde{\gamma}_v = (2\beta_d \bar{\mathcal{D}}^\omega - \tilde{C}_1)^2.$$

in (99) while the other terms are unchanged.

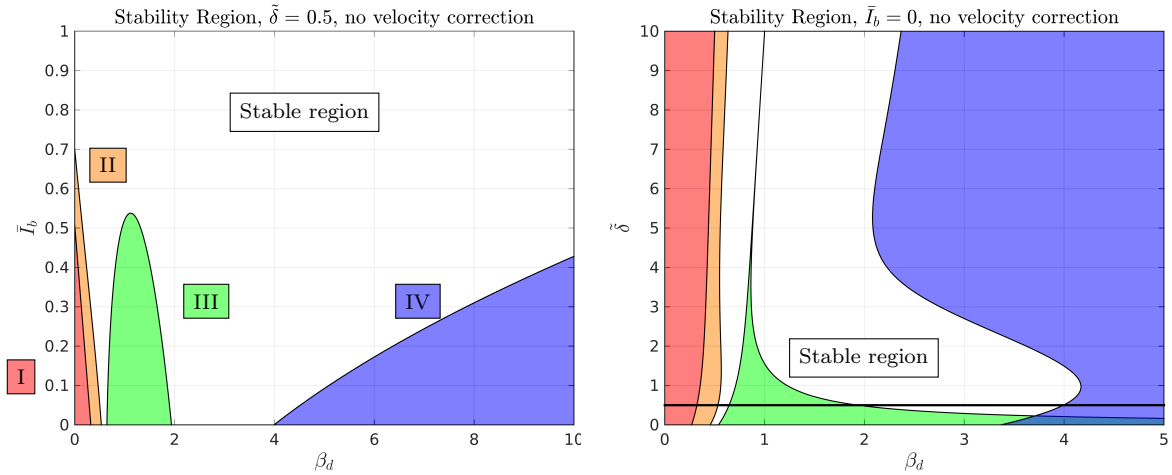

Figure 9: Stability regions for the AMP-RB scheme without velocity correction for the added-damping model problem in an annular geometry. Left: stability region in the β_d–$\bar{I}_b$ plane for $\tilde{\delta} = .5$; shaded unstable regions are marked according to the form of the instability. Right: stability region in the β_d–$\tilde{\delta}$ plane for the zero-mass body. Here $r_1 = 20\sqrt{\nu \Delta t/2}$ and $r_2 = 2\, r_1$.

The stability regions for the annular case are not as straightforward to investigate as the prior rectangular case because (98) and (99) are transcendental functions, and so the number of roots is not known a-priori. Nonetheless, the use of the argument principle reveals that there are a finite number of roots with $|A| > 1$ for a given choice of parameters $(\bar{I}_b, \tilde{\delta}, \beta_d)$. Using this information we are able to identify locations where the number of unstable roots changes, and from these points we perform a simple numerical continuation to trace out the stability boundaries.

Plots of the stability region for the AMP-RB scheme without the velocity-correction step are shown in Figure 9, while those for the scheme with velocity-correction are shown in Figure 10. Comparing to the corresponding plots for the rectangular geometry in Figures 4 and 5, it is clear that the stability regions for the annular geometry are very similar in form to those for the rectangular geometry. For example, the AMP-RB-NVC scheme has four regions of instability, and the stability region for the AMP-RB-VC scheme shows similar improvements as in the rectangular geometry with the troublesome instability region III no longer present. Perhaps the most important conclusion to be drawn from Figure 10 is that there is again a large range for β_d, near $\beta_d = 1$, where the AMP-RB-VC is stable for any non-negative value of the scaled moment of inertia $\bar{I}_b$. This allows one to pick $\beta_d = 1$ and obtain a robustly stable FSI algorithm. Finally

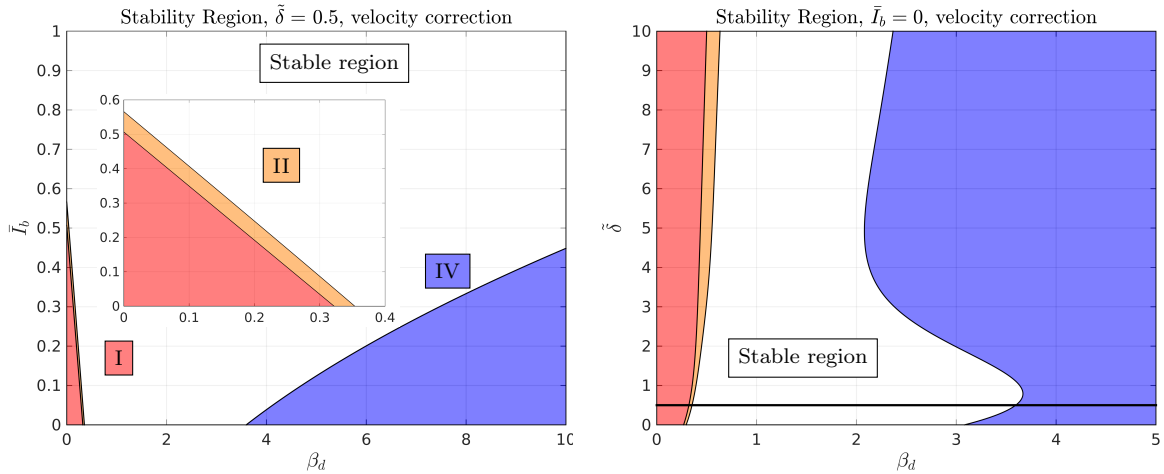

Figure 10: Stability regions for the AMP-RB scheme with velocity correction for the added-damping model problem in an annular geometry. Left: stability region in the β_d–$\bar{I}_b$ plane for $\tilde{\delta} = .5$; shaded unstable regions are marked according to the form of the instability. Right: stability region in the β_d–$\tilde{\delta}$ plane for the zero-mass body. Here $r_1 = 20\sqrt{\nu \Delta t/2}$ and $r_2 = 2\, r_1$.

we note that the traditional-partitioned scheme corresponds to $\beta_d = 0$, and has a similar behaviour to that found for the rectangular geometry.

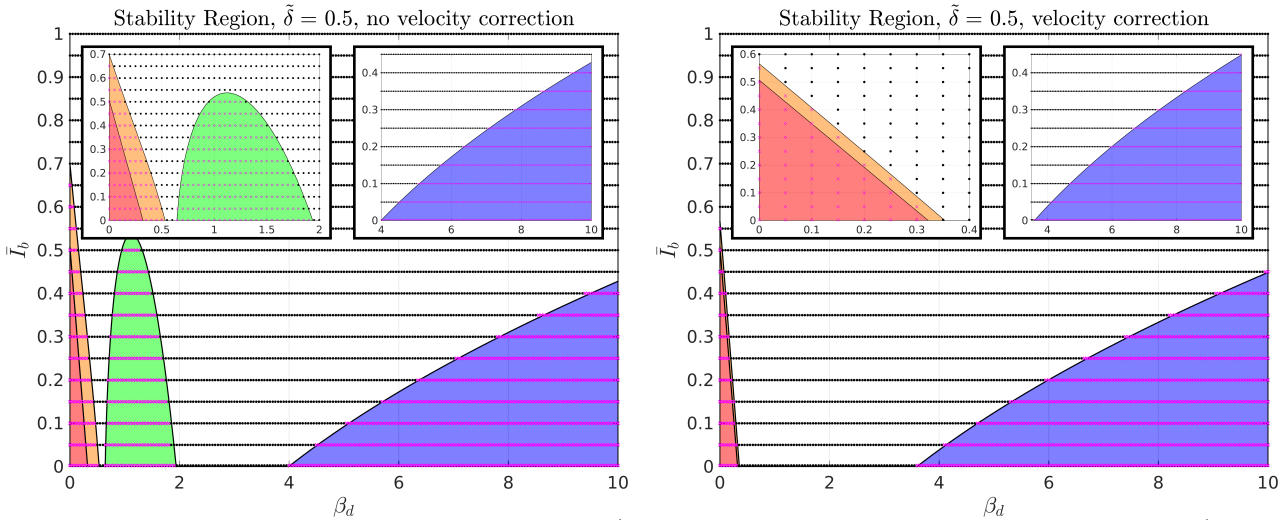

Figure 11: Numerically determined points of stability (black dots for stable and magenta crosses for unstable) compared to the theoretical stability region for the added-damping model problem in an annular geometry. Left:the AMP-RB-NVC scheme. Right: the AMP-RB-VC scheme.

Figure 11 shows values of the parameters where the AMP-RB schemes are numerically determined to be stable or unstable for the annular geometry. The numerical stability results are computed in a similar fashion to those for the rectangular grid case (see Section 5.2.3). The computational grid is chosen to be the curvilinear grid $\mathcal{G}^{(4)}$, as defined in Section 7.4, and the time-step is taken as $\Delta t = 0.05$. In this annular geometry case, the theoretical results used continuous spatial differential operators except in the interface conditions, while the numerical results use a fully discrete approximation. Despite this difference, the points where the numerical scheme is stable or unstable are in excellent agreement with the theory.

7. Numerical verification

In this section, numerical simulations are used to confirm the results of the stability analyses, and to demonstrate the second-order accuracy of the AMP-RB scheme by comparison to some exact solutions. Calculations with rigid bodies having a range of masses are presented, but the focus is on light or zero-mass bodies where added-damping and added-mass effects are most significant. We note that the zero-mass case is representative of cases in which the mass of the body is very small since the results are nearly identical.

The numerical results are organized into four sections. Section 7.1 considers the one-dimensional motion of a rigid rectangular *piston* moving into an adjacent incompressible fluid, This case corresponds to the added-mass model problem MP-AM, and the results demonstrate stability and second-order accuracy for a range of rigid-body masses. Then in Section 7.2, results for the one-dimensional added-damping model problem MP-AD of a rectangular body sliding against an incompressible fluid are presented, and again the results show stability and second-order accuracy for a range of rigid body masses. In addition, by adjusting the added damping parameter, β_d, we are able to numerically demonstrate the existence of the different instability modes that were predicted by the analysis discussed in Section 5.2.3. Subsequently in Sections 7.3 and 7.4, the stability and accuracy of the AMP-RB scheme in a two-dimensional annular geometry are demonstrated for two problems involving a translating disk and a rotating disk. In these last two cases the motion of the disk in the numerical solution is free to translate and rotate, and thus both added-mass and added-damping effects can be important and are tested in the scheme.

7.1. Piston motion of a rigid body and an incompressible fluid

Consider the added-mass model problem in a rectangular geometry (MP-AM) with fluid domain $\Omega = [0, L] \times [0, H]$, where $L = H = 1$, and the fluid density is $\rho = 1$. The fluid domain is discretized using a uniform grid, denoted by $\mathcal{G}^{(j)}$, with time-step and grid spacing given by $\Delta t^{(j)} = \Delta y^{(j)} = 1/(10j)$. The fluid pressure boundary condition at $y = H$ is $p(H, t) = p_H(t)$, and there is no external body forcing, i.e., $g_v(t) = 0$. The rigid body has mass m_b, which is varied in the numerical results. The exact solution to this system is given in (28)–(30), and the applied pressure $p_H(t)$ is chosen from (28) so that the rigid body undergoes a specified motion given by $y_b(t) = \frac{1}{4}\sin(2\pi t)$.

Figure 12 shows the position, velocity and acceleration of the rigid body computed on the grid $\mathcal{G}^{(4)}$ using the AMP-RB scheme with $m_b = 1$ and $m_b = 0$. The exact solution is independent of the rigid-body mass, and so the two numerical approximations are nearly identical. Figure 12 also presents the errors in the approximations of the position, velocity and acceleration of the rigid body for $\mathcal{G}^{(4)}$.

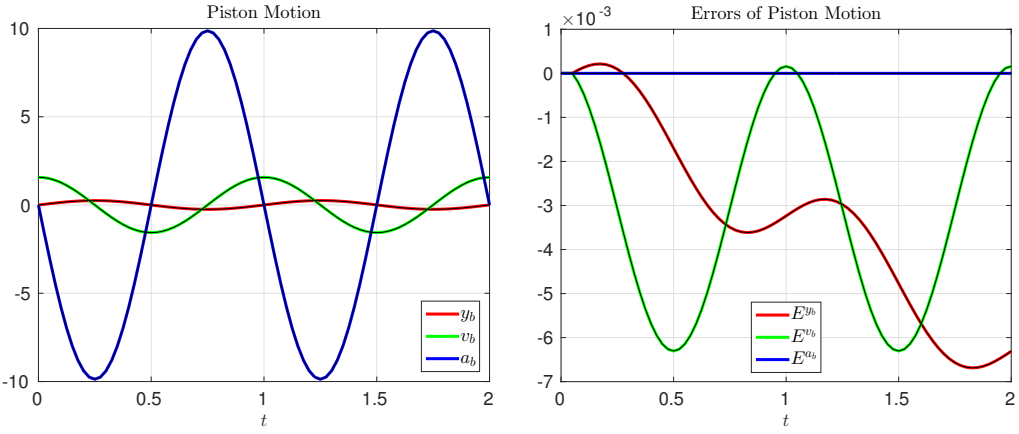

Figure 12: Piston motion. Stable solutions and errors for the motion of a medium, $m_b = 1$, and massless, $m_b = 0$ (black lines), rigid body. The grid used is $\mathcal{G}^{(4)}$.

A grid convergence study is performed for the AMP-RB scheme, and the results are presented in Table 1. In the tables, E_j^p, $E_j^{\mathbf{v}}$, etc., denote the maximum-norm errors in p, $\mathbf{v}$, etc., on grid $\mathcal{G}^{(j)}$. The convergence rates in the final row of each table are computed using a least squares fit to the log of the errors. Three cases are presented in Table 1, corresponding to a heavy body, $m_b = 10$, medium body, $m_b = 1$, and massless

body, $m_b = 0$. In all cases, second-order accuracy is demonstrated for the position and velocity of the body and the velocity of the fluid, while the fluid pressure and the acceleration of the body are exact to machine precision, as predicted by the theory. Note also that the observed errors in the position and velocities are nearly identical for all rigid-body masses because the exact solution is the same for all cases. Finally note that the second-order accurate TP-RB scheme is found to be unstable when the added-mass ratio $M_r \lesssim 1$, which matches the theory for the TP-RB scheme as presented in Section 5.

Piston motion, $m_b = 10$										
$\Delta y^{(j)}$	E_j^p	r	$E_j^{\mathbf{v}}$	r	$E_j^{\mathbf{x}_b}$	r	$E_j^{\mathbf{v}_b}$	r	$E_j^{\mathbf{a}_b}$	r
1/20	3.1e-13		6.5e-3		1.4e-2		6.5e-3		3.0e-14	
1/40	8.8e-13		2.1e-3	3.1	3.6e-3	3.8	2.1e-3	3.1	8.7e-14	
1/80	2.6e-13		5.5e-4	3.8	9.0e-4	4.0	5.5e-4	3.8	2.5e-14	
1/160	2.5e-12		1.4e-4	3.9	2.2e-4	4.0	1.4e-4	3.9	2.5e-13	
rate			1.85		1.98		1.85			

Piston motion, $m_b = 1$										
$\Delta y^{(j)}$	E_j^p	r	$E_j^{\mathbf{v}}$	r	$E_j^{\mathbf{x}_b}$	r	$E_j^{\mathbf{v}_b}$	r	$E_j^{\mathbf{a}_b}$	r
1/20	7.1e-15		6.5e-3		1.4e-2		6.5e-3		1.8e-15	
1/40	5.2e-14		2.1e-3	3.1	3.6e-3	3.8	2.1e-3	3.1	5.2e-14	
1/80	2.8e-13		5.5e-4	3.8	9.0e-4	4.0	5.5e-4	3.8	2.1e-13	
1/160	1.4e-13		1.4e-4	3.9	2.2e-4	4.0	1.4e-4	3.9	1.2e-13	
rate			1.85		1.98		1.85			

Piston motion, $m_b = 0$										
$\Delta y^{(j)}$	E_j^p	r	$E_j^{\mathbf{v}}$	r	$E_j^{\mathbf{x}_b}$	r	$E_j^{\mathbf{v}_b}$	r	$E_j^{\mathbf{a}_b}$	r
1/20	1.8e-15		6.5e-3		1.4e-2		6.5e-3		0.0e0	
1/40	3.1e-14		2.1e-3	3.1	3.6e-3	3.8	2.1e-3	3.1	6.0e-14	
1/80	2.6e-14		5.5e-4	3.8	9.0e-4	4.0	5.5e-4	3.8	9.4e-14	
1/160	4.8e-14		1.4e-4	3.9	2.2e-4	4.0	1.4e-4	3.9	1.5e-13	
rate			1.85		1.98		1.85			

Table 1: Piston motion. Maximum errors and estimated convergence rates at $t = 0.8$ computed using the AMP-RB scheme for a heavy, $m_b = 10$, medium, $m_b = 1$, and massless, $m_b = 0$, rigid body. The column labeled "r" provides the ratio of the errors at the current grid spacing to that on the next coarser grid.

7.2. A rigid body sliding against an incompressible fluid

Turning now to the situation where added-damping effects are dominant, consider the added-damping model problem (MP-AD) for the same square domain used in the previous case. For this problem the fluid boundary condition at $y = H$ is taken as a no-slip condition $u(H, t) = 0$, and there is no external forcing, $g_u(t) = 0$, as before. In this case, an exact solution is given by

$$u = -\frac{\sin(\lambda(y - H))}{\sin(\lambda H)}\, e^{-\nu\lambda^2 t},$$

where λ is an eigenvalue determined by a solution of the transcendental equation

$$\lambda H \tan(\lambda H) = \frac{\rho L H}{m_b} = \frac{1}{M_r}.$$

Note that there are infinitely many solutions to this equation, and the numerical tests use the smallest positive eigenvalue, as given in Table 2 for a few values of M_r.

	$M_r = 10$	$M_r = 1$	$M_r = 10^{-3}$	$M_r = 0$
λH	0.311052848200298	0.860333589019380	1.56922710098197	1.57079632679489

Table 2: Scaled eigenvalues, λH, in the exact solution of the sliding block problem for different values of M_r.

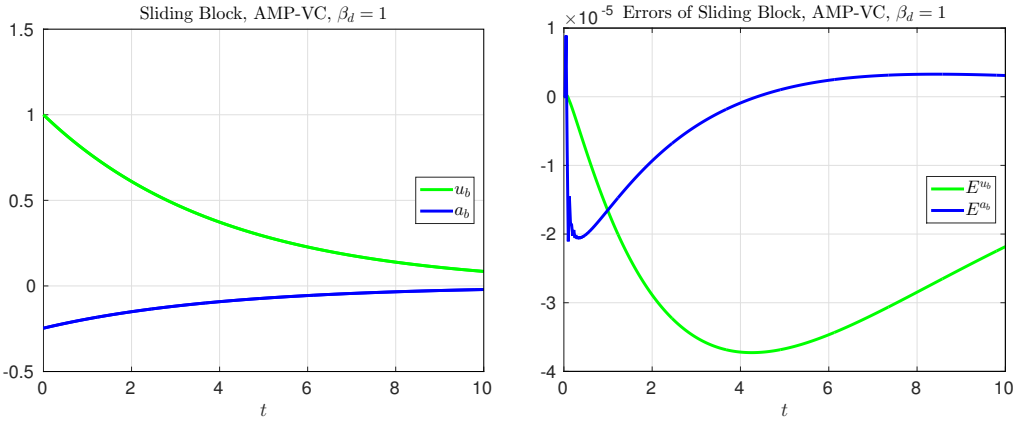

Figure 13: Sliding block. Stable solutions and errors for the motion of a massless, $m_b = 0$, body. The AMP-RB-VC scheme on the grid $\mathcal{G}^{(4)}$ is used with $\beta_d = 1$.

Sliding block, $m_b = 10$						
$\Delta y^{(j)}$	$E_j^{\mathbf{v}}$	r	$E_j^{\mathbf{v}_b}$	r	$E_j^{\mathbf{a}_b}$	r
1/20	7.0e-7		7.0e-7		7.4e-7	
1/40	1.9e-7	3.8	1.9e-7	3.8	1.9e-7	4.0
1/80	4.6e-8	4.0	4.6e-8	4.0	4.6e-8	4.0
1/160	1.2e-8	4.0	1.2e-8	4.0	1.2e-8	4.0
1/320	2.9e-9	4.0	2.9e-9	4.0	2.9e-9	4.0
1/640	7.4e-10	4.0	7.4e-10	4.0	7.2e-10	4.0
rate	1.98		1.98		2.00	

Sliding block, $m_b = 1$						
$\Delta y^{(j)}$	$E_j^{\mathbf{v}}$	r	$E_j^{\mathbf{v}_b}$	r	$E_j^{\mathbf{a}_b}$	r
1/20	3.3e-5		3.3e-5		3.0e-5	
1/40	8.5e-6	3.9	8.5e-6	3.9	7.2e-6	4.1
1/80	2.1e-6	4.1	2.1e-6	4.1	1.8e-6	4.0
1/160	5.2e-7	4.0	5.2e-7	4.0	4.4e-7	4.0
1/320	1.3e-7	4.0	1.3e-7	4.0	1.1e-7	4.0
1/640	3.3e-8	4.0	3.3e-8	4.0	2.8e-8	4.0
rate	1.99		1.99		2.01	

Sliding block, $m_b = 0$						
$\Delta y^{(j)}$	$E_j^{\mathbf{v}}$	r	$E_j^{\mathbf{v}_b}$	r	$E_j^{\mathbf{a}_b}$	r
1/20	6.1e-5		3.7e-5		5.6e-5	
1/40	1.9e-5	3.2	1.7e-5	2.1	1.6e-5	3.4
1/80	5.2e-6	3.6	5.1e-6	3.3	4.4e-6	3.7
1/160	1.4e-6	3.7	1.4e-6	3.7	1.1e-6	3.9
1/320	3.6e-7	3.9	3.6e-7	3.8	2.9e-7	3.9
1/640	9.3e-8	3.9	9.3e-8	3.9	7.3e-8	4.0
rate	1.88		1.76		1.92	

Table 3: Sliding block. Maximum errors and estimated convergence rates at $t = 1$ computed using the AMP-RB-VC scheme for a heavy, $m_b = 10$, medium, $m_b = 1$, and massless, $m_b = 0$, rigid body.

Figure 13 shows the velocity and acceleration (and errors in the same) of a massless rigid body, $m_b = 0$, with $\nu = 0.1$ on grid $\mathcal{G}^{(4)}$ as computed by the AMP-RB-VC with $\beta_d = 1$. Results from grid convergence studies using the AMP-RB-VC scheme with $\beta_d = 1$ are presented in Table 3 and demonstrate second-order accuracy for massless, medium, and heavy rigid bodies. As in the prior convergence study the time step is taken as $\Delta t^{(j)} = \Delta y^{(j)} = 1/(10j)$. Also note that the second-order accurate TP-RB scheme is found to be unstable when $m_b \lesssim 0.653$ at $\delta = 0.5$, which agrees with the theoretical prediction of $m_b \leq 0.656$ from (77).

Next we probe the classifications of unstable modes as discussed in Section 5.2. Figure 14 shows computed results for the AMP-RB scheme where the added-damping parameter β_d is intentionally chosen to elicit the unstable behaviour of a type typified by one of the four instability regimes. The plots in the top row of

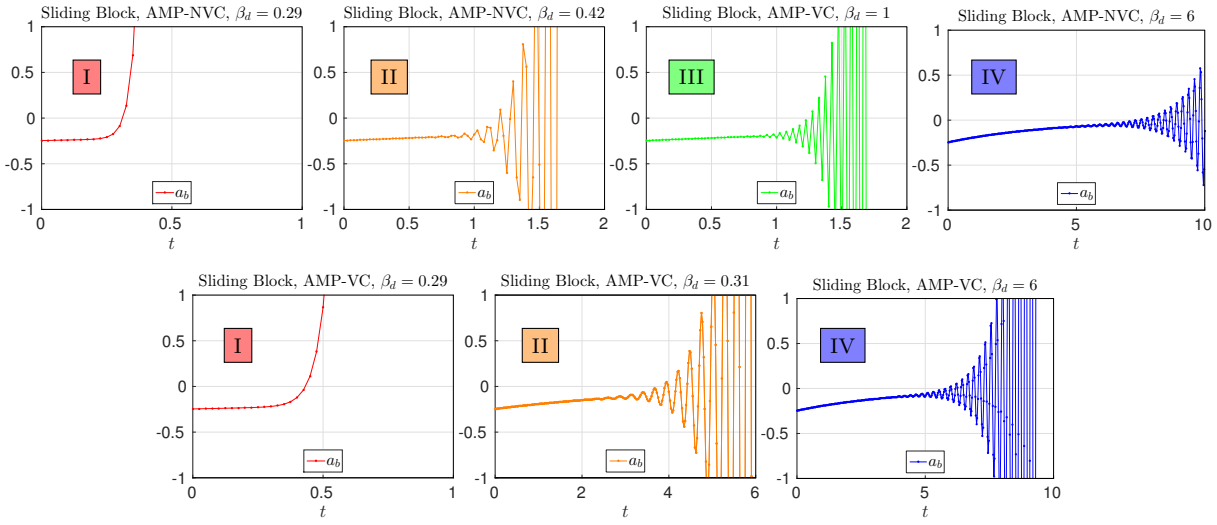

Figure 14: Sliding block. Acceleration of a light rigid body with $m_b = 0.001$. Top: typical instabilities in the AMP-RB-NVC scheme: (I) for $\beta_d = 0.29$ there is a rapid, monotonically growing instability; (II) for $\beta_d = 0.42$ there is a rapidly growing, high-frequency instability; (III) for $\beta_d = 1$ there is a rapidly growing, step-to-step oscillatory instability; and (IV) for $\beta_d = 6$ there is a slowly growing, low-frequency instability. Bottom: typical instabilities in the AMP-RB-VC scheme: (I) for $\beta_d = 0.29$ there is a rapid, monotonically growing instability; (II) for $\beta_d = 0.31$ there is a rapidly growing, high-frequency instability; and (IV) for $\beta_d = 6$ there is a slowly growing, low-frequency instability.

the figure show results for the AMP-RB-NVC scheme, while the plots in the bottom row show results for the AMP-RB-VC scheme. By comparing the behaviour of the computed instabilities with those predicted by the stability analysis (see Figures 4 and 5), we find the numerical results are in excellent agreement with the results of the theory for all modes of instability.

7.3. Translating disk in an incompressible fluid

To discuss added-mass effects and the AMP-RB scheme in a two-dimensional setting, consider the translation of a rigid disk of radius $r_1 = 1$ surrounded by an annular fluid region bounded by a radius $r_2 = 2$ (see Figure 8). The interface matching conditions are applied on the surface of the disk at $r = r_1$ and a no-slip boundary condition is taken on the outer boundary $r = r_2$. An exact solution to this problem can be derived assuming an infinitesimal displacement of the body. The analysis, as described in Appendix A, seeks solutions with the horizontal velocity of the rigid body taken to be

$$u_b(t) = \alpha_b e^{-\lambda^2 \nu t},$$

where α_b is the (small) amplitude of the motion, λ is an eigenvalue and $\nu = \mu/\rho$ is the kinematic viscosity. The corresponding fluid velocity and pressure in this solution have the form

$$\mathbf{v}(r,\theta,t) = (\hat{Q}(r)/r) \begin{bmatrix} \cos^2\theta \\ \sin\theta\cos\theta \end{bmatrix} e^{-\lambda^2\nu t} + \hat{Q}'(r) \begin{bmatrix} \sin^2\theta \\ -\sin\theta\cos\theta \end{bmatrix} e^{-\lambda^2\nu t},$$
$$p(r,\theta,t) = \mu\,(A_p r + B_p/r)\, e^{-\lambda^2\nu t}\cos\theta + p_0,$$

where (r,θ) are polar coordinates, $\hat{Q}(r)$ is given in (A.9), A_p and B_b are constant specified in the exact solution, and p_0 is an arbitrary constant. The eigenvalues λ are determined from (A.11) and the smallest (positive) values are given in Table A.7 for various choices of the density ρ_b of the solid disk (see Appendix A).

In the numerical tests to follow, the amplitude of the horizontal motion is taken as $\alpha_b = 10^{-7}$ (to approximately satisfy the assumption of infinitesimal displacement), and the arbitrary constant p_0 is set to zero. The inner and outer radii of the annular fluid domain are taken to be $r_1 = 1$ and $r_2 = 2$, respectively,

and the density and viscosity of the fluid are $\rho = 1$ and $\mu = 0.1$. The values of λ used for the exact solution, and the corresponding initial conditions for the simulations, are taken from Table A.7. The annular grids used in the computations are denoted by $\mathcal{G}^{(j)}$ and have grid spacing $\Delta r^{(j)} = 1/(10j)$ and $\Delta\theta^{(j)} = 2\pi/(60j)$. The time step is taken as $\Delta t^{(j)} = 1/(10j)$.

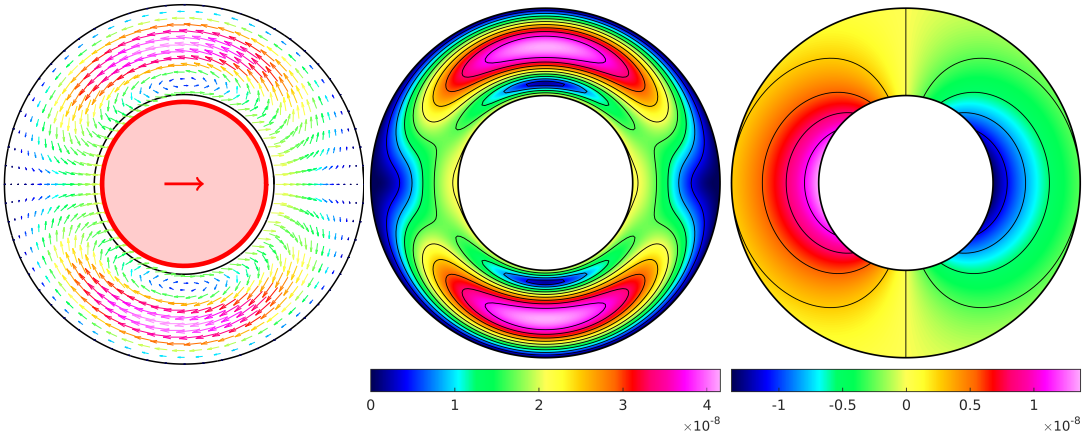

Figure 15: Translating disk. Computed velocity vectors (left), speed (middle) and pressure (right) using the grid $\mathcal{G}^{(4)}$ for $\rho_b = 0$. The color bar below the middle plot also applied to the left plot.

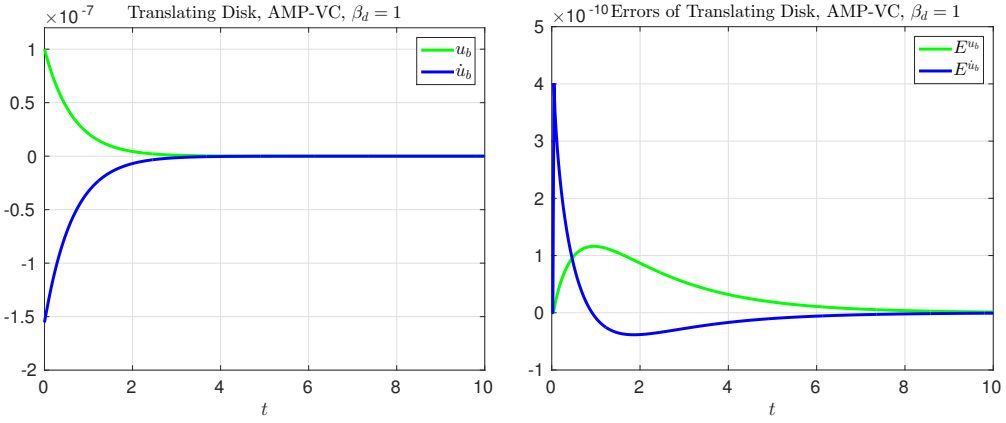

Figure 16: Translating disk. Velocity and acceleration of the body (left) and errors (right) for a massless, $\rho_b = 0$, rigid disk using the grid $\mathcal{G}^{(4)}$. The AMP-RB-VC scheme is used with $\beta_d = 1$.

Figures 15 and 16 illustrate the behaviour of the solution for a massless rigid body ($\rho_b = 0$) as determined by the AMP-RB-VC scheme using $\mathcal{G}^{(4)}$. Note that although the exact solution to this test case has no rotation, the numerical implementation allows the full set of motions including both x and y translations as well as rotation. As such it is important to include stabilization against added-damping effects and this is done by including the added-damping terms with $\beta_d = 1$. Results from a convergence study are provided in Table 4, which demonstrate second-order accuracy for all choices of body densities, ρ_b.

7.4. Rotating disk in a disk of incompressible fluid

In this final example we consider a rotating solid disk surrounded by an annular fluid region. Rotational added-damping effects play an important role in this problem. The geometry of the problem and the grid for the fluid domain are identical to those given in Section 7.3. The interface matching conditions are applied on the surface of the disk, $r_1 = 1$, and no-slip boundary conditions are imposed on the fixed outer boundary, $r_2 = 2$. The fluid density and viscosity are taken to be $\rho = 1$ and $\mu = 0.1$.

Translating disk, $\rho_b = 10$								
$\Delta r^{(j)}$	E_j^p	r	$E_j^{\mathbf{v}}$	r	$E_j^{\mathbf{v}_b}$	r	$E_j^{\dot{\mathbf{v}}_b}$	r
1/10	4.1e-9		2.0e-9		6.1e-10		6.0e-10	
1/20	1.2e-9	3.5	5.8e-10	3.5	1.7e-10	3.5	1.7e-10	3.5
1/40	3.0e-10	3.9	1.6e-10	3.7	4.9e-11	3.6	4.5e-11	3.8
1/80	7.6e-11	4.0	4.1e-11	3.8	1.3e-11	3.8	1.2e-11	3.9
1/160	1.9e-11	4.0	1.0e-11	3.9	3.3e-12	3.9	2.9e-12	3.9
rate	1.94		1.90		1.88		1.92	

Translating disk, $\rho_b = 1$								
$\Delta r^{(j)}$	E_j^p	r	$E_j^{\mathbf{v}}$	r	$E_j^{\mathbf{v}_b}$	r	$E_j^{\dot{\mathbf{v}}_b}$	r
1/10	2.1e-10		9.7e-10		9.7e-10		2.7e-10	
1/20	6.3e-11	3.3	2.6e-10	3.8	2.6e-10	3.8	7.4e-11	3.7
1/40	1.8e-11	3.5	6.7e-11	3.9	6.7e-11	3.9	1.6e-11	4.6
1/80	4.8e-12	3.7	1.7e-11	3.9	1.7e-11	3.9	3.5e-12	4.6
1/160	1.2e-12	3.9	4.3e-12	4.0	4.3e-12	4.0	8.6e-13	4.1
rate	1.86		1.96		1.96		2.10	

Translating disk, $\rho_b = 0$								
$\Delta r^{(j)}$	E_j^p	r	$E_j^{\mathbf{v}}$	r	$E_j^{\mathbf{v}_b}$	r	$E_j^{\dot{\mathbf{v}}_b}$	r
1/10	2.9e-10		1.7e-9		1.7e-9		8.0e-11	
1/20	8.8e-11	3.3	4.5e-10	3.7	4.5e-10	3.7	1.7e-11	4.7
1/40	2.3e-11	3.8	1.2e-10	3.9	1.2e-10	3.9	9.1e-12	1.9
1/80	5.8e-12	3.9	2.9e-11	4.0	2.9e-11	4.0	3.2e-12	2.9
1/160	1.5e-12	3.9	7.4e-12	4.0	7.4e-12	4.0	8.3e-13	3.8
rate	1.92		1.96		1.96		1.56	

Table 4: Translating disk. Maximum errors and estimated convergence rates at $t = 1$ computed using the AMP-RB-VC scheme for a heavy, $\rho_b = 10$, medium, $\rho_b = 1$, and massless, $\rho_b = 0$, rigid disk.

An exact solution can be found for a disk rotating about its centre assuming there is no displacement of the disk in the x or y directions. If there is no external torque on the disk, then a straightforward application of separation of variables leads to a solution of the form

$$\mathbf{v}(r,\theta,t) = v_\theta(r,t)\begin{bmatrix}-\sin\theta\\ \cos\theta\end{bmatrix}, \qquad p(r,t) = \rho\int_{r_1}^{r}\frac{[v_\theta(s,t)]^2}{s}\,ds + p_0,$$

where p_0 is a constant and

$$v_\theta(r,t) = \alpha_b\left[\frac{J_1(\lambda r)Y_1(\lambda r_2) - J_1(\lambda r_2)Y_1(\lambda r)}{J_1(\lambda r_1)Y_1(\lambda r_2) - J_1(\lambda r_2)Y_1(\lambda r_1)}\right]e^{-\lambda^2\nu t},$$

is the circumferential component of the velocity. Here, J_1 and Y_1 are Bessel functions of order one and α_b is the velocity at $r = r_1$ and $t = 0$. The angular velocity of the rigid body in the exact solution is given by

$$\omega_b(t) = \frac{v_\theta(r_1,t)}{r_1} = \frac{\alpha_b e^{-\lambda^2\nu t}}{r_1}.$$

We note that the solution decays at a rate determined by the eigenvalues λ for which there are an infinite number. These eigenvalues satisfy a constraint determined from the equation for the angular acceleration of the body. This constraint has the form

$$\left[\frac{\partial v}{\partial r} - \left[\frac{1}{r_1} - \frac{\lambda^2 I_b}{2\pi\rho r_1^3}\right]v\right]_{r=r_1} = 0,$$

where I_b is the moment of inertia of the solid disk. Assuming a disk with uniform density, ρ_b, we have $I_b = \rho_b\pi r_1^4/2$, and the smallest (positive) values of λ are given in Table 5 for various values of ρ_b. We note

that unlike the solution described in Appendix A for the infinitesimal motion of a translating disk, the solution given here for the rotating disk is an exact solution of the full Navier-Stokes equations for any value of the amplitude α_b.

	$\rho_b = 10$	$\rho_b = 1$	$\rho_b = 10^{-3}$	$\rho_b = 0$
λ	0.969674911038943	1.97045369767466	2.27309495331973	2.27340628201175

Table 5: Eigenvalues, λ, in the exact solution of the rotating disk for different values of ρ_b.

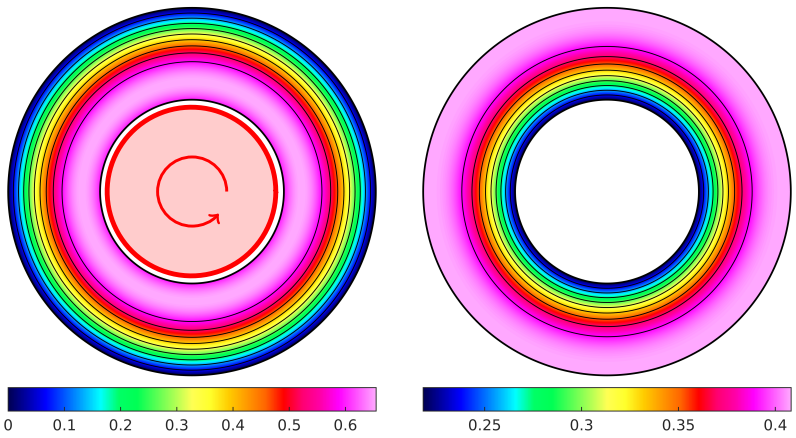

Figure 17: Rotating disk. Computed speed (left) and pressure (right) for a massless disk, $\rho_b = 0$, using the grid $\mathcal{G}^{(4)}$. The AMP-RB-VC scheme is used with $\beta_d = 1$.

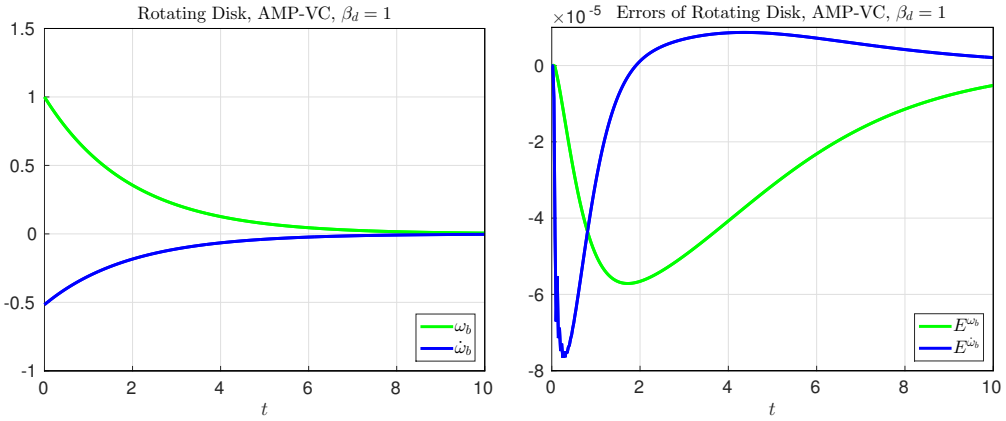

Figure 18: Rotating disk. Angular velocity and acceleration (left) and errors (right) of a massless disk, $\rho_b = 0$, using the grid $\mathcal{G}^{(4)}$. The AMP-RB-VC scheme is used with $\beta_d = 1$.

Figures 17 shows shaded contours of the speed and pressure of the fluid at $t = 1$, while Figure 18 shows the behaviour of the angular velocity and acceleration of the disk along with the errors in these quantities. The solution illustrated in these two figures is computed for a massless disk ($\rho_b = 0$) using the AMP-RB-VC scheme on the grid $\mathcal{G}^{(4)}$ with $\beta_d = 1$. In addition, Table 6 presents the errors at $t = 1$ and estimated convergence rates for simulations with $\rho_b = 0$, 1, and 10. These convergence rates demonstrate the second-order accuracy of the AMP-RB approach even for the difficult case of a massless body in which added-damping effects are strong. While the exact solution for the rigid body assumes only rotation, the numerical implementation does not make this assumption so that both rotation and translation of the body

Rotating disk, $\rho_b = 10$								
$\Delta r^{(j)}$	E_j^p	r	$E_j^{\mathbf{v}}$	r	$E_j^{\omega_3}$	r	$E_j^{\dot{\omega}_3}$	r
1/10	3.9e-3		1.5e-3		4.3e-4		4.4e-4	
1/20	1.1e-3	3.6	4.3e-4	3.4	1.2e-4	3.5	1.3e-4	3.4
1/40	2.8e-4	3.9	1.2e-4	3.6	3.5e-5	3.5	3.5e-5	3.7
1/80	7.1e-5	4.0	3.2e-5	3.8	9.3e-6	3.7	9.1e-6	3.8
1/160	1.8e-5	4.0	8.1e-6	3.9	2.4e-6	3.9	2.3e-6	3.9
rate	1.95		1.88		1.87		1.90	

Rotating disk, $\rho_b = 1$								
$\Delta r^{(j)}$	E_j^p	r	$E_j^{\mathbf{v}}$	r	$E_j^{\omega_3}$	r	$E_j^{\dot{\omega}_3}$	r
1/10	3.7e-4		1.1e-3		2.7e-4		5.8e-5	
1/20	1.0e-4	3.7	3.1e-4	3.6	4.1e-5	6.6	2.2e-5	2.6
1/40	2.6e-5	3.8	8.1e-5	3.9	6.7e-6	6.0	6.7e-6	3.3
1/80	6.6e-6	3.9	2.1e-5	3.9	1.2e-6	5.5	1.8e-6	3.7
1/160	1.7e-6	3.9	5.2e-6	4.0	2.5e-7	4.9	4.6e-7	3.8
rate	1.95		1.95		2.51		1.76	

Rotating disk, $\rho_b = 0$								
$\Delta r^{(j)}$	E_j^p	r	$E_j^{\mathbf{v}}$	r	$E_j^{\omega_3}$	r	$E_j^{\dot{\omega}_3}$	r
1/10	1.2e-3		1.2e-3		4.2e-4		5.3e-4	
1/20	3.6e-4	3.2	3.4e-4	3.6	1.6e-4	2.5	1.3e-4	4.0
1/40	9.5e-5	3.8	9.0e-5	3.8	5.0e-5	3.3	3.0e-5	4.4
1/80	2.4e-5	4.0	2.3e-5	3.9	1.4e-5	3.7	7.0e-6	4.3
1/160	6.1e-6	3.9	5.8e-6	4.0	3.5e-6	3.9	1.7e-6	4.0
rate	1.91		1.94		1.74		2.07	

Table 6: Rotating disk. Maximum errors and estimated convergence rates at $t = 1$ computed using the AMP-RB scheme for a heavy, $\rho_b = 10$, medium, $\rho_b = 1$ and massless, $\rho_b = 0$, rigid disk.

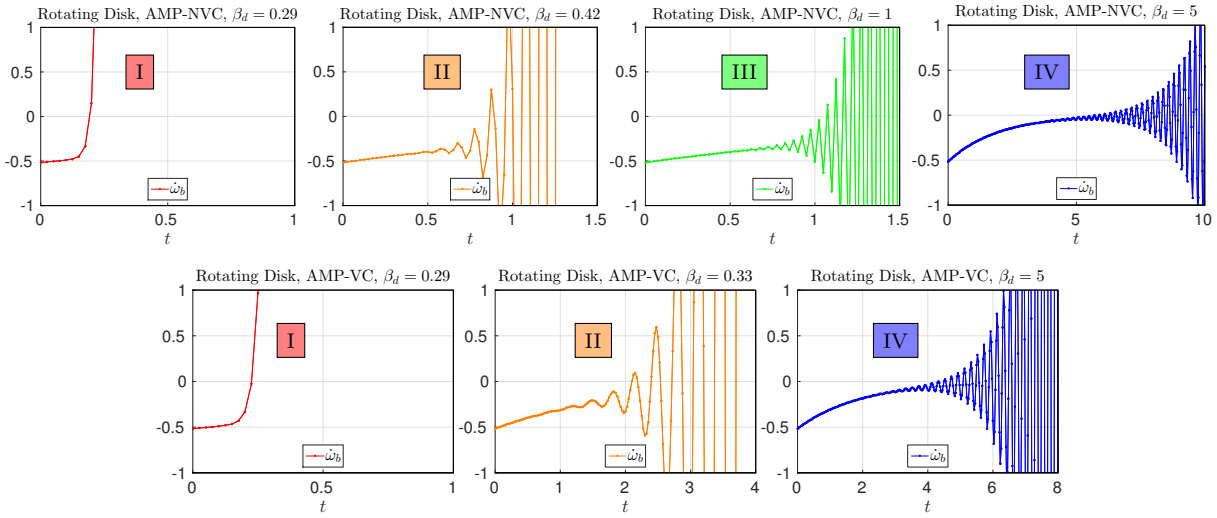

Figure 19: Rotating disk. Angular acceleration of a rotating light rigid body with $\rho_b = 0.001$ using the grid $\mathcal{G}^{(4)}$. Top: typical instabilities in the AMP-RB-NVC scheme: (I) for $\beta_d = 0.29$ there is a rapid, monotonically growing instability; (II) for $\beta_d = 0.42$ there is a rapidly growing, high-frequency instability; (III) for $\beta_d = 1$ there is a rapidly growing, step-to-step instability; and (IV) for $\beta_d = 5$ there is a slowly growing, low-frequency instability. Bottom: typical instabilities in the AMP-RB-VC scheme: (I) for $\beta_d = 0.29$ there is a rapid, monotonically growing instability; (II) for $\beta_d = 0.33$ there is a rapidly growing, high-frequency instability; and (IV) for $\beta_d = 5$ there is a slowly growing, low-frequency instability.

are allowed. Therefore, it is important to include stabilization against added-mass effects, as discussed previously, although the computed translational velocities are very close to zero (in good agreement with

the exact solution).

Finally, we probe the classifications of unstable modes, similar to what was done in the the prior case of the sliding block in Section 7.2. Figure 19 presents time traces of the angular acceleration for a very light rigid body with $\rho_b = 0.001$ computed using the grid $\mathcal{G}^{(4)}$. Different values of the added-damping parameter β_d are used to elicit unstable behaviours of the various types. Even though the AMP-RB-VC scheme is stable for a range of values of β_d about $\beta_d = 1$ as predicted by the theory and demonstrated in previous figures, instabilities occur in the AMP-RB-VC and AMP-RB-NVC schemes for values of β_d outside the stability region. We observe that the behaviours of the instabilities shown in Figure 19 are in good agreement with those predicted by the analysis of Section 6.

8. Conclusions

In this first part of a two-part series, a partitioned scheme for simulating fluid structure interactions between incompressible flows and rigid bodies is developed and analyzed. This new AMP-RB scheme is stable, without sub-time-step iterations, for bodies of any mass, including bodies of zero mass. A fractional-step time-stepping scheme is used to evolve the incompressible fluid where the velocity and pressure are solved in separate stages. Coupling of the rigid-body equations occurs in the pressure equation where the degrees of freedom corresponding to rigid-body accelerations are solved in conjunction with the fluid pressure, and both added-mass and added-damping effects are effectively addressed by the AMP-RB scheme. Added-mass effects are treated with a generalized Robin interface condition that couples the fluid pressure and body accelerations. Added-damping effects are handled by introducing an added-damping coefficient into the equations of motion for the rigid body. The form of this added-damping coefficient (which in general geometries becomes an added-damping tensor) is derived from a linearization of the integrals that define the force and torques on the body. An approximate form for the added-damping coefficient, suitable for use with general bodies, is determined from a local analysis and variational problem.

The stability properties of the proposed interface conditions are studied for a rectangular-geometry and an annular-geometry model-problem using mode analysis. The analyses of the model problems for added-mass effects show that the AMP-RB scheme is stable for bodies of any mass including bodies of zero mass. On the other hand, the analysis of the added-damping model problem reveals that for very light bodies a final velocity-correction stage should be used to ensure stability. The mode analysis is used to determine the values for the stabilizing added-damping parameter β_d (which scales the added-damping coefficient) to ensure stability of the scheme. It is shown that there is range of values for β_d where the scheme remains stable independent of the problem parameters ν, Δt, grid spacing, body mass, and body moment-of-inertia. As a result the parameter β_d can chosen once and for all and does not need to be adjusted from problem to problem. With this additional correction phase, the AMP-RB scheme is shown to be stable against added-damping effects for any body mass, including the zero mass case.

Numerical results are provided for model problems in rectangular and annular geometries that confirm the results of the theoretical analyses. These results verify stability and second-order accuracy of the AMP-RB scheme, including for bodies of zero mass. Part II of this work considers the extension of the AMP-RB scheme to general geometries.

Appendix A. Exact solution for a translating disk in an annular Stokes flow

An exact solution to an FSI problem involving the horizontal motion of a solid disk in an incompressible Stokes flow is described. The solution is used in Section 7.3 to access the accuracy of the AMP-RB scheme for an FSI problem in an annular geometry. The configuration of the problem is shown in Figure 8 and the equations governing the motion of the body and the velocity and pressure of the fluid are given in (79)–(85). As before, we assume that the amplitude of the motion is small and linearize the problem about the fixed

interface at $r = r_1$. Using the transformation of the fluid variables in (87), the governing equations become

$$\text{Fluid:} \quad \rho\frac{\partial \hat{u}}{\partial t} + \frac{\partial \hat{p}}{\partial r} = \mu\left[\frac{1}{r}\frac{\partial}{\partial r}\left(r\frac{\partial \hat{u}}{\partial r}\right) - \frac{2\hat{u}}{r^2} + \frac{2\hat{v}}{r^2}\right], \quad r_1 < r < r_2, \tag{A.1}$$

$$\rho\frac{\partial \hat{v}}{\partial t} + \frac{\hat{p}}{r} = \mu\left[\frac{1}{r}\frac{\partial}{\partial r}\left(r\frac{\partial \hat{v}}{\partial r}\right) - \frac{2\hat{v}}{r^2} + \frac{2\hat{u}}{r^2}\right], \quad r_1 < r < r_2, \tag{A.2}$$

$$\frac{\partial}{\partial r}(r\hat{u}) - \hat{v} = 0, \quad r_1 < r < r_2, \tag{A.3}$$

$$\text{Rigid body:} \quad m_b\frac{du_b}{dt} = r_1\pi\left[-\hat{p} + \mu\frac{\partial \hat{v}}{\partial r}\right]\Big|_{r=r_1}, \tag{A.4}$$

$$\text{Interface:} \quad \hat{u}(r_1, t) = \hat{v}(r_1, t) = u_b(t), \tag{A.5}$$

$$\text{Fluid BCs:} \quad \hat{u}(r_2, t) = \hat{v}(r_2, t) = 0. \tag{A.6}$$

Here, we have assumed that the body does not rotate so that $\omega_b(t) = 0$ and that there is no external force on the body, i.e. $g_u(t) = 0$. The equations are homogeneous and the motion is initiated by the (non-zero) initial conditions which we specify later.

Separable solutions of the linear equations for the fluid in (A.1)–(A.3) have the form

$$\hat{p}(r, t) = \mu\left(A_p r + \frac{B_p}{r}\right)e^{-\lambda^2\nu t}, \tag{A.7}$$

and

$$\hat{u}(r, t) = \left(\frac{\hat{Q}(r)}{r}\right)e^{-\lambda^2\nu t}, \qquad \hat{v}(r, t) = \hat{Q}'(r)e^{-\lambda^2\nu t}, \tag{A.8}$$

where

$$\hat{Q}(r) = A_1 J_1(\lambda r) + B_1 Y_1(\lambda r) + \frac{1}{\lambda^2}\left(A_p r - \frac{B_p}{r}\right). \tag{A.9}$$

Here, J_1 and Y_1 are Bessel functions of order one, $\nu = \mu/\rho$ is the kinematic viscosity, and A_p, B_p, A_1 and B_1 are constants. For later purposes, define the following constants:

$$b_{11} = \frac{\pi r_2}{2r_1}\Big(2Y_1(\lambda r_2) - \lambda r_2 Y_0(\lambda r_2)\Big), \qquad b_{12} = \frac{\pi}{2}\lambda r_1 Y_0(\lambda r_2),$$
$$b_{21} = \frac{\pi r_2}{2r_1}\Big(2J_1(\lambda r_2) - \lambda r_2 J_0(\lambda r_2)\Big), \qquad b_{22} = \frac{\pi}{2}\lambda r_1 J_0(\lambda r_2),$$

and

$$c_{11} = \frac{b_{11}J_1(\lambda r_1) - b_{21}Y_1(\lambda r_1) + 1}{\lambda^2 r_1^2}, \qquad c_{12} = \frac{b_{12}J_1(\lambda r_1) - b_{22}Y_1(\lambda r_1) - 1}{\lambda^2 r_1^2},$$
$$c_{21} = \frac{b_{11}\lambda r_1 J_1'(\lambda r_1) - b_{21}\lambda r_1 Y_1'(\lambda r_1) + 1}{\lambda^2 r_1^2}, \qquad c_{22} = \frac{b_{12}\lambda r_1 J_1'(\lambda r_1) - b_{22}\lambda r_1 Y_1'(\lambda r_1) + 1}{\lambda^2 r_1^2}.$$

Using (A.8) in the boundary conditions (A.5) and (A.6), together with identities for Bessel functions, gives

$$A_1 = \frac{1}{r_1\lambda^2}\left[r_1^2 b_{11}A_p + b_{12}B_p\right], \qquad B_1 = -\frac{1}{r_1\lambda^2}\left[r_1^2 b_{21}A_p + b_{22}B_p\right],$$

and

$$A_p = \frac{\alpha_b}{r_1^2}\left[\frac{c_{22} - c_{12}}{c_{11}c_{22} - c_{12}c_{21}}\right], \qquad B_p = \alpha_b\left[\frac{c_{11} - c_{21}}{c_{11}c_{22} - c_{12}c_{21}}\right],$$

where α_b is the (small) amplitude of the velocity of the body given by

$$u_b(t) = \alpha_b e^{-\lambda^2\nu t}. \tag{A.10}$$

Finally, using (A.7), (A.8) and (A.10) in the equation governing the motion of the rigid body (A.4) gives the transcendental equation

$$\frac{m_b}{\rho\pi}\lambda^2 + \left[-1 + b_{11}J_1''(\lambda r_1) - b_{21}Y_1''(\lambda r_1)\right]\left[\frac{c_{22}-c_{12}}{c_{11}c_{22}-c_{12}c_{21}}\right] + \left[-1 + b_{12}J_1''(\lambda r_1) - b_{22}Y_1''(\lambda r_1) - \frac{2}{\lambda^2 r_1^2}\right]\left[\frac{c_{11}-c_{21}}{c_{11}c_{22}-c_{12}c_{21}}\right] = 0, \tag{A.11}$$

which determines the eigenvalues λ of the separable solutions.

There are an infinite number of solutions of (A.11) for a given set of parameters of the problem. We are interested in the smallest (positive) value of λ which corresponds to the solution with the slowest rate of decay. For example, if $m_b = \rho_b \pi r_1^2$, $\rho = 1$, $r_1 = 1$ and $r_2 = 2$, then the smallest values of λ can be computed by solving (A.11) numerically for different values of ρ_b. Some of these solutions are collected in Table A.7. Finally, the initial conditions for the problem are taken from (A.8) and (A.10) for a computed value of λ upon setting $t = 0$.

	$\rho_b = 10$	$\rho_b = 1$	$\rho_b = 10^{-3}$	$\rho_b = 0$
λ	1.84604165628237	3.40692142656753	3.94155013131292	3.94219755667612

Table A.7: Eigenvalues, λ, in the exact solution of the translating disk for different values of ρ_b.

References

[1] N. Takashi, T. J. Hughes, An arbitrary Lagrangian-Eulerian finite element method for interaction of fluid and a rigid body, Comput. Method. Appl. Mech. Engrg. 95 (1) (1992) 115–138.

[2] H. H. Hu, N. A. Patankar, M. Y. Zhu, Direct numerical simulations of fluid-solid systems using the arbitrary langrangian-eulerian technique, J. Comput. Phys. 169 (2) (2001) 427–462.

[3] J. Vierendeels, K. Dumont, E. Dick, P. Verdonck, Analysis and stabilization of fluid-structure interaction algorithm for rigid-body motion, AIAA J. 43 (12) (2005) 2549–2557.

[4] M. Coquerelle, G.-H. Cottet, A vortex level set method for the two-way coupling of an incompressible fluid with colliding rigid bodies, J. Comput. Phys. 227 (21) (2008) 9121–9137.

[5] F. Gibou, C. Min, Efficient symmetric positive definite second-order accurate monolithic solver for fluid/solid interactions, J. Comput. Phys. 231 (8) (2012) 3246–3263.

[6] R. Glowinski, T.-W. Pan, T. I. Hesla, D. D. Joseph, A distributed Lagrange multiplier/fictitious domain method for particulate flows, Int. J. Multiphase Flow 25 (5) (1999) 755–794.

[7] R. Glowinski, T.-W. Pan, T. I. Hesla, D. D. Joseph, J. Périaux, A distributed Lagrange multiplier/fictitious domain method for the simulation of flow around moving rigid bodies: application to particulate flow, Comput. Method. Appl. Mech. Engrg. 184 (2) (2000) 241–267.

[8] R. Glowinski, T. W. Pan, T. I. Hesla, D. D. Joseph, J. Périaux, A fictitious domain approach to the direct numerical simulation of incompressible viscous flow past moving rigid bodies: Applications to particulate flow, J. Comput. Phys. 169 (2001) 363–426.

[9] S. D. Costarelli, L. Garelli, M. A. Cruchaga, M. A. Storti, R. Ausensi, S. R. Idelsohn, An embedded strategy for the analysis of fluid structure interaction problems, Comput. Method. Appl. Mech. Engrg. 300 (2016) 106–128.

[10] T. Kajishima, S. Takiguchi, Interaction between particle clusters and particle-induced turbulence, Int. J. Heat Fluid Flow 23 (5) (2002) 639–646.

[11] M. Uhlmann, An immersed boundary method with direct forcing for the simulation of particulate flows, J. Comput. Phys. 209 (2) (2005) 448–476.

[12] D. Kim, H. Choi, Immersed boundary method for flow around an arbitrarily moving body, J. Comput. Phys. 212 (2) (2006) 662–680.

[13] T.-R. Lee, Y.-S. Chang, J.-B. Choi, D. W. Kim, W. K. Liu, Y.-J. Kim, Immersed finite element method for rigid body motions in the incompressible Navier–Stokes flow, Comput. Method. Appl. Mech. Engrg. 197 (25) (2008) 2305–2316.

[14] I. Borazjani, L. Ge, F. Sotiropoulos, Curvilinear immersed boundary method for simulating fluid structure interaction with complex 3D rigid bodies, J. Comput. Phys. 227 (16) (2008) 7587–7620.

[15] W.-P. Breugem, A second-order accurate immersed boundary method for fully resolved simulations of particle-laden flows, J. Comput. Phys. 231 (13) (2012) 4469–4498.

[16] T. Kempe, J. Fröhlich, An improved immersed boundary method with direct forcing for the simulation of particle laden flows, J. Comput. Phys. 231 (9) (2012) 3663–3684.

[17] J. Yang, F. Stern, A simple and efficient direct forcing immersed boundary framework for fluid–structure interactions, J. Comput. Phys. 231 (15) (2012) 5029–5061.

[18] A. P. S. Bhalla, R. Bale, B. E. Griffith, N. A. Patankar, A unified mathematical framework and an adaptive numerical method for fluid–structure interaction with rigid, deforming, and elastic bodies, J. Comput. Phys. 250 (2013) 446–476.

[19] J. Yang, F. Stern, A non-iterative direct forcing immersed boundary method for strongly-coupled fluid–solid interactions, J. Comput. Phys. 295 (2015) 779–804.

[20] C. Wang, J. D. Eldredge, Strongly coupled dynamics of fluids and rigid-body systems with the immersed boundary projection method, J. Comput. Phys. 295 (2015) 87–113.

[21] Y. Kim, C. S. Peskin, A penalty immersed boundary method for a rigid body in fluid, Phys. Fluids 28 (3) (2016) 033603.

[22] U. Lācis, K. Taira, S. Bagheri, A stable fluid–structure-interaction solver for low-density rigid bodies using the immersed boundary projection method, J. Comput. Phys. 305 (2016) 300–318.

[23] C. Conca, A. Osses, J. Planchard, Added mass and damping in fluid–structure interaction, Comput. Method. Appl. Mech. Engrg. 146 (3-4) (1997) 387–405.

[24] A. Robinson-Mosher, C. Schroeder, R. Fedkiw, A symmetric positive definite formulation for monolithic fluid structure interaction, J. Comput. Phys. 230 (4) (2011) 1547–1566.

[25] S. Badia, A. Quaini, A. Quarteroni, Splitting methods based on algebraic factorization for fluid–structure interaction, SIAM J. Sci. Comput. 30 (4) (2008) 1778–1805.

[26] W. D. Henshaw, A fourth-order accurate method for the incompressible Navier-Stokes equations on overlapping grids, J. Comput. Phys. 113 (1) (1994) 13–25.

[27] W. D. Henshaw, N. A. Petersson, A split-step scheme for the incompressible Navier-Stokes equations, in: M. M. Hafez (Ed.), Numerical Simulation of Incompressible Flows, World Scientific, 2003, pp. 108–125.

[28] J. W. Banks, W. D. Henshaw, D. W. Schwendeman, Q. Tang, A stable partitioned FSI algorithm for rigid bodies and incompressible flow. Part II: General formulation, preprint arXiv:1611.05703, arXiv, submitted for publication (2016).

[29] W. D. Henshaw, D. W. Schwendeman, Moving overlapping grids with adaptive mesh refinement for high-speed reactive and non-reactive flow, J. Comput. Phys. 216 (2) (2006) 744–779.

[30] J. W. Banks, W. D. Henshaw, B. Sjögreen, A stable FSI algorithm for light rigid bodies in compressible flow, J. Comput. Phys. 245 (2013) 399–430.

[31] J. W. Banks, W. D. Henshaw, D. W. Schwendeman, Deforming composite grids for solving fluid structure problems, J. Comput. Phys. 231 (9) (2012) 3518–3547.

[32] J. W. Banks, W. D. Henshaw, A. Kapila, D. W. Schwendeman, An added-mass partitioned algorithm for fluid-structure interactions of compressible fluids and nonlinear solids, J. Comput. Phys. 305 (2016) 1037–1064.

[33] J. W. Banks, W. D. Henshaw, D. W. Schwendeman, An analysis of a new stable partitioned algorithm for FSI problems. Part I: Incompressible flow and elastic solids, J. Comput. Phys. 269 (2014) 108–137.

[34] J. W. Banks, W. D. Henshaw, D. W. Schwendeman, An analysis of a new stable partitioned algorithm for FSI problems. Part II: Incompressible flow and structural shells, J. Comput. Phys. 268 (2014) 399–416.

[35] L. Li, W. D. Henshaw, J. W. Banks, D. W. Schwendeman, G. A. Main, A stable partitioned FSI algorithm for incompressible flow and deforming beams, J. Comput. Phys. 312 (2016) 272–306.

[36] N. A. Petersson, Stability of pressure boundary conditions for Stokes and Navier-Stokes equations, J. Comput. Phys. 172 (1) (2001) 40–70.

[37] B. Gustafsson, H.-O. Kreiss, A. Sundström, Stability theory of difference approximations for mixed initial boundary value problems. II, Mathematics of Computation 26 (119) (1972) 649–686.